

REPORT DOCUMENTATION PAGE

AFRL-SR-AR-TR-05-

0016

Public reporting burden for this collection of information is estimated to average 1 hour per response, including the time for reviewing instructions, data needed, and completing and reviewing this collection of information. Send comments regarding this burden estimate or any other aspect of this burden to Department of Defense, Washington Headquarters Services, Directorate for Information Operations and Reports (0704-0188), 4302. Respondents should be aware that notwithstanding any other provision of law, no person shall be subject to any penalty for failing to comply with a valid OMB control number. PLEASE DO NOT RETURN YOUR FORM TO THE ABOVE ADDRESS.

1. REPORT DATE (DD-MM-YYYY) 24-12-2004		2. REPORT TYPE Final Technical Report		3. DATES COVERED (From - To) From 6/2001 to 2/2004
4. TITLE AND SUBTITLE (THEME 3) Meso and Micro Scale Propulsion Concepts for Small Spacecraft				5a. CONTRACT NUMBER
				5b. GRANT NUMBER F49620-01-1-0376
6. AUTHOR(S) R.A. Yetter [†] , V. Yang [*] , I. A. Aksay [*] and F.L. Dryer [*]				5c. PROGRAM ELEMENT NUMBER
				5d. PROJECT NUMBER
				5e. TASK NUMBER
7. PERFORMING ORGANIZATION NAME(S) AND ADDRESS(ES) [†] Department of Mechanical and Nuclear Engineering The Pennsylvania State University University Park, PA 16802 [*] Department of Chemical Eng. Aerospace Engineering Princeton University Princeton, NJ 08544				5f. WORK UNIT NUMBER
				8. PERFORMING ORGANIZATION REPORT NUMBER
				10. SPONSOR/MONITOR'S ACRONYM(S)
9. SPONSORING / MONITORING AGENCY NAME(S) AND ADDRESS(ES) AFOSR ATTN: Dr. Mitat Birkan 801 North Randolph Street Room 732 Arlington, VA 22203-1977				11. SPONSOR/MONITOR'S REPORT NUMBER(S)
				NE
12. DISTRIBUTION / AVAILABILITY STATEMENT Unlimited Distribution				
20050125 137				
13. SUPPLEMENTARY NOTES				
14. ABSTRACT <p>A meso/micro scale liquid propellant thruster was designed and developed for small spacecraft. Gas-phase combustion was stabilized in small combustion chambers (~10-200 mm³) using vortex flows. For liquid propellant steady-state operation, the propellant was injected directly into the chamber tangentially along the combustor wall. Heat feedback from the flame, once ignited, decomposed and gasified the liquid propellant. Although the propellant of interest was a HAN based liquid propellant, initial studies were conducted with liquid nitromethane. Operation of the combustion chamber with pure nitromethane at a chamber pressure of 8 atm was achieved. To gasify and initially ignite a HAN based propellant, techniques that make use of the electrolytic character of the propellant were investigated. In particular, exposure of small liquid droplets to voltage drops of ~ 10 volts were shown to initiate electrochemical reactions and eventually thermal reactions that gasify and in some instances ignited the droplet. Implementation of this concept into the microthruster was estimated to reduce power requirements and improve thermal management during ignition. Combustion chambers and nozzles were fabricated from ceramics (alumina) because of the required high flame temperatures required to sustain gas-phase reaction. Operation of thrusters on hydrogen – air – oxygen mixtures at combustion chamber pressures as high as 8 atm was demonstrated to produce characteristic velocity efficiencies of approximately 90%.</p>				
15. SUBJECT TERMS Meso and Micro Scale Combustion and Propulsion, Electrolytic Ignition, Ceramic Stereolithography				
16. SECURITY CLASSIFICATION OF: Unclassified		17. LIMITATION OF ABSTRACT	18. NUMBER OF PAGES	19a. NAME OF RESPONSIBLE PERSON Richard A. Yetter
a. REPORT	b. ABSTRACT	c. THIS PAGE	51	19b. TELEPHONE NUMBER (include area code) (814) 863-6375

Executive Summary

The objectives of this research program were to design, fabricate, and test chemical micro-thrusters for propulsion of small and micro-spacecraft. The key features of the effort were: (1) the use of novel, environmentally friendly, liquid propellant formulations, (2) the simplicity of the design as a result of the choice of propellants, (3) detailed modeling, coordinated with the design and testing of the micro-propulsion components and system, (4) the use of micro-scale combustion and fluid dynamics diagnostics for testing and evaluation, and (5) the fabrication of meso and micro scale, 3-dimensional, uni-body combustion chambers and nozzles from ceramics using stereolithography techniques. The propellant formulations under consideration included new energetic oxidizers (hydrazinium nitroformate, ammonium dinitramide, and hydroxylammonium nitrate), alcohol fuels, and water as the liquid carrier. The following significant accomplishments have been made during this effort.

Asymmetric Combustion in Small Volumes:

- Demonstrated vortex flame stabilization in small volumes as a means to obtain sustained gas-phase combustion over a wide range of operating conditions and extended duration.
- Performed experimental scaling studies of combustion in small volumes ranging from 10 to 170 mm³.
- Demonstrated small-volume vortex-combustion chamber operation with non-premixed gaseous mixtures of hydrogen/air, methane/air, and propane/air.
- Demonstrated continuous combustion of nitromethane, a liquid monopropellant, by making use of tangential injection into the vortex chamber and wall vaporization.

Numerical Modeling of Combustion in Small Volumes:

- Developed three-dimensional numerical codes for analysis of both non-reacting and reacting flows in small-volume vortex-combustion chambers.
- Performed cold-flow computational parametric studies to understand the detailed flow structures in vortex combustion chambers with various configurations.
- Performed reacting flow simulations with gaseous hydrogen and hydrocarbons to study flame stabilization mechanisms and flame spreading processes.

Electrolytic Ignition of Liquid Propellants:

- Demonstrated electrolytic ignition concept as a means to gasify, decompose, and in some instances ignite HAN-based liquid propellants.
- Characterized the electrolytic gasification and thermal decomposition of HAN-based propellants via suspended droplet experiments, photographic observations, and measurement of gasification times, droplet resistance and power consumption.

Fabrication and Diagnostic Testing of Meso Scale Ceramic Thrusters:

- Fabricated the first axisymmetric meso-scale thrusters from ceramics using stereolithography techniques.
- Characterized non-reacting and reacting meso-scale thruster operations via measurements of chamber pressure, chamber temperature, and characteristic velocity.
- Demonstrated thruster operation in both continuous and pulsed modes.
- Analyzed plume structure by shadowgraph and schlieren techniques.
- Characterized downstream plume velocity vectors by particle image velocimetry.

Table of Contents

Abstract	1
Executive Summary	2
Table of Contents	3
Introduction	4
Scaling and Combustion Issues	6
Research Objectives	9
Results	10
Asymmetric Whirl Combustion in Small Volumes	10
Model Development and Analysis of Vortex Flows	22
Electrolytic Ignition	26
Thruster Design and Fabrication	34
Thruster Operation and Characterization	36
Summary and Future Research	42
Technology Transfer	45
Publications and Presentations	47
References	48

Introduction

Two developing technology areas in the field of microelectromechanical systems (MEMS) are micropower generation and micropropulsion [1-5]. Microthrusters, because of their simplicity, have received significant attention during the last few years, although early development in the MEMS field began approximately 10 years ago [8-16]. The principle applications of microthrusters are for primary propulsion and attitude control of microspacecraft, but they may also be applied to any process requiring small quantities of directed gas flows. For example, the same technology necessary for the successful development of micro-thrusters is currently being applied to micro gas generators for usage in airbags and in microactuators [17-19].

As a recent example of the development of micro-spacecraft and the need for micro-thrusters, the US Air Force's XSS-10 microsatellite experiment flew on 29 January 2003 as a secondary payload to a Global Positioning System navigation satellite aboard a Delta 2 rocket [20]. The micro-satellite weighed 28 kilograms and represented the first work in space involving micro-satellites that can autonomously approach other objects in space. The experiment was also the first in which the Air Force activated the satellite hours after the launch versus a normal on-orbit checkout ranging from weeks to months. Shortly after reaching space, the XSS-10 spacecraft maneuvered about 200 meters away from the rocket, and then approached it, taking video imagery that was transmitted live to the ground. The experiment also provided information that researchers are now incorporating into follow on missions called XSS-11, which is a yearlong test of microsatellite technologies. More importantly, the XSS-10 experiment represented a significant step in transforming the way the Air Force can operate in space.

For solid propellant rockets, the interest in microthrusters results from the potential gain in thrust-to-weight ratio (F/W) with downsizing. Thrust is proportional to the characteristic length squared, $F \propto P_c A_t \propto \ell^2$, where P_c is the combustion chamber pressure and A_t is the nozzle throat cross-sectional area. Because initial weight of a solid propellant thruster is approximately proportional to volume (ℓ^3), the thrust-to-weight ratio is inversely proportional to length scale ($F/W \propto \ell^{-1}$). Thus, if a one-meter macro-scale thruster has a thrust-to-weight ratio of 10, a thruster with a length scale of 1 cm could potentially have a thrust-to-weight ratio of 1000 and a thruster with a length scale of 1 mm could have a thrust-to-weight ratio of 10,000. If achievable, the applications of microthrusters could be numerous, ranging from distributed propulsion in macro-scale systems to primary propulsion in micro-scale systems. Although potential gains are

also expected with scaling of liquid and gas thrusters, such scaling is not as simplistic as with solid propellant thrusters and therefore may not directly apply.

Of the various possible macroscale rocket systems, cold-gas, chemical and electrical thrusters are scalable and have been under study at the micro-scale. Chemical thrusters are generally divided into liquid and solid propellant systems with liquid propellant thrusters further divided into monopropellant and bipropellant systems. **Table 1** provides a list of various examples of thrusters currently under development at the meso- and micro-scales along with literature references.

Table 1. Examples of Meso and Micro-Scale Chemical Thrusters Under Development	
Type	References
Bipropellant Micro Rocket	[21], [22]
Monopropellant Micro Rocket	[23], [24], [25], [26]
Solid Fuel Micro Rocket	[5], [27], [28], [29], [30]
Gas Micro Thruster	[5], [31]
Vaporizing Micro Rocket	[5], [26], [32]

This report describes the design, fabrication and testing of a chemical microthruster under development at the Pennsylvania State University and Princeton University and supported by AFOSR. Prior to describing the results of this program, scaling issues important to propulsion and combustion are first addressed to provide a preliminary analysis for the initial microthruster design. From this analysis, some general features of the microthruster were selected: including the use of environmentally friendly, liquid propellant formulations, electrolytic ignition for primary ignition or ignition assistance, asymmetric whirl combustion for gas-phase combustion stabilization, and ceramic stereolithography for fabrication of meso- and micro-scale, 3-dimensional, uni-body combustion chambers and nozzles.

Scaling and Combustion Issues

The effects of miniaturization on the fluid mechanics, heat transfer, and combustion characteristics involved in micropower devices have been recently analyzed by Fernandez-Pello [6]. These same considerations are relevant to operation of chemical micropropulsion devices. In addition, a scaling analysis of chemical microthrusters based on simple 1-D isentropic relationships describing rocket engine performance and on 1-D flame structure physics has been reported by Bruno [33] and Bruno et al. [34]. Scaling implications of flows in micro nozzles have also been studied [14,15,16,35]. Here, we briefly discuss some of the effects of decreasing the characteristic length scale, ℓ , of thrusters.

When compared to macroscale systems, microthrusters will operate at lower Re ($U\ell/v$) and Pe ($U\ell/\alpha$) numbers. Consequently, viscous and diffusive effects will play a greater role. The flows will be less turbulent and laminar conditions will generally prevail. Boundary conditions, which are usually not very influential in large-scale systems, will play a more significant role at smaller scales. Diffusive processes, which in micron-sized channels can be fast, will largely dominate species mixing but in millimeter sized combustion chambers can be too slow to be effective. Although the greater viscous forces will result in larger pumping requirements, certain advantages such as reduced leakage of gases through micron-sized joints may be achieved. Higher viscous losses also imply that larger Re 's numbers are needed at smaller length scales to achieve a desired thrust [34]. One approach to achieve high Re numbers in micro thrusters will be to operate at high pressure.

As viscosity becomes more and more important with continued downsizing, the simple isentropic expansion expressions used in conventional thruster design will apply less and less. For example, measured Isp of rocket micronozzles was found to decrease by a factor of 10 when the nozzle Re was reduced from 4000 to 400 by decreasing the size [12,34]. In addition, Alexeenko et al. [35] have performed both Navier-Stokes and DSMC calculations on 2D planar and 2D axisymmetric nozzles and found that the flow in the 2D flat nozzles was indeed 3D and produced ~20% less thrust than a 2D axisymmetric nozzle, in which the surface-to-cross sectional area ratio is minimized. Unfortunately, traditional silicon-based MEMS fabrication techniques are limited to producing 2D planar structures.

Lower specific impulses are expected due to lower combustion chamber temperatures resulting from enhanced heat transfer losses and increased viscous losses with downsizing. For example, a comparison of heat loss rate ($\dot{Q}_{loss} \propto \ell^{1.5}$) to heat generation rate ($\dot{Q}_{gen} \propto \ell^3$) yields

$\dot{Q}_{\text{loss}} / \dot{Q}_{\text{gen}} \propto \ell^{-1.5}$. Depending upon the dominant mode of heat transfer at the external surface, this scaling may vary, but the ratio will increase with miniaturization. Thus, downsizing without effective means to recover lost energy will result in lower combustion temperatures and hence lower Isp.

As length scale is decreased, velocity, temperature and species gradients at boundaries will increase, producing larger momentum, energy and mass transport rates near the surfaces and making it difficult to maintain large differences between the wall and bulk flow variables. Considering heat transfer, Biot numbers ($h\ell/k_s$) associated with microstructures will generally be much less than unity, resulting in nearly uniform body temperatures. Fourier numbers ($\alpha t/\ell^2$) indicate that thermal response times of structures will be small. Alexeenko et al. [36] have performed transient DSMC coupled thermal and fluid analysis of microthruster flows in 2D and 3D planar nozzles and found that at any instant in time after start-up, the silicon thruster body was nearly uniform in temperature and that heat was transferred from the combustion chamber flow to the nozzle diffuser flow through the thruster body. Temperatures of the thruster with an adiabatic external surface and initial body temperature of 300 K were predicted to reach 1200 K after ~ 13 s of operation. Because view factors increase with decreasing characteristic length, radiative heat transfer will also play a significant role in chemical thrusters.

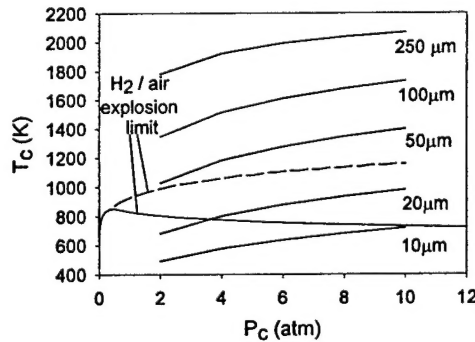


Figure 1. Effect of reducing throat diameter of a meso-scale thruster on combustion temperature.

Figure 1 shows results from a 1D analysis of a small-scale thruster operating on a stoichiometric hydrogen-air mixture. In the analysis, steady-state conditions, complete combustion, and choked flow at the nozzle orifice were all assumed. In addition, the nozzle flow was assumed to be isentropic and the Biot Number < 0.1 . As a result, the temperature in the combustion chamber was assumed equal to the wall temperature of the thruster body. For the results shown, the outer dimensions of the thruster were kept constant as well as the combustion chamber volume. The overall dimensions of the thruster body were 1 cm^3 with a combustor

volume of $\sim 150 \text{ mm}^3$. Scaling was investigated by decreasing the nozzle orifice diameter from 250 to 10 μm . Consequently, the mass flow rate was also reduced thus increasing the ratio of $\dot{Q}_{\text{loss}} / \dot{Q}_{\text{gen}}$ by lowering \dot{Q}_{gen} . For this particular analysis, it is evident that when the throat diameter approaches 20 μm , combustion will not be sustainable because the chamber temperature is reduced below the explosion limit temperatures of the mixture.

For efficient combustion, the residence time ($\tau_R \propto \ell/U$) must be greater than the chemical time (τ_C). The ratio of these times is a Damköhler number (τ_R / τ_C). In general, τ_R will decrease with decreasing ℓ and therefore to sustain combustion, chemical times will also need to be reduced. As mentioned above, increased surface-to-volume ratios make this difficult because of the increase in $\dot{Q}_{\text{loss}} / \dot{Q}_{\text{gen}}$. The high surface-to-volume ratio and small length scales favor catalytic combustion at small ℓ . Catalytic combustion is generally slower than gas-phase combustion and deposits energy directly into the thruster body. For efficient gas-phase combustion, high inlet, wall, and combustion temperatures for increased kinetic rates, operation with stoichiometric mixtures, and use of highly energetic fuels are all approaches to enhance combustion.

The times of physical processes such as mixing and liquid fuel evaporation also need to be reduced with ℓ if efficient combustion is to be achieved. For sprays, droplet sizes need to be reduced to shorten evaporation times, which implies greater pressure and energy requirements for atomization. To address this aspect, micro-electrospray atomizers are being considered [37,38]. An alternative approach under investigation is to use film-cooling techniques as a means to introduce liquid fuels into the combustion chamber, since surface-to-volume ratios are high [39].

Other processes that have increased importance at small length scales such as thermal creep (transpiration) and electrokinetic effects are also being considered for use in microthrusters. For example, transpiration effects are currently being investigated by Ochoa et al. [40] to supply fuel to microthrusters creating an *in-situ* thermally driven propellant flow at the front end of the combustor. Clearly, there are many opportunities for combustion research at the microscale to facilitate the design of microthrusters. Although not discussed here, the research, design, and manufacturing of other components of microthruster systems, such as valves and pumps, remain equally important science and technology areas [5]. In fact, the availability of high pressure, leak tight, MEMS valves that consume minimal power is currently one of the limiting factors in chemical micro-thruster development.

Research Objectives

The objectives of this proposal were to design, fabricate and test micro-thrusters for small spacecraft based on the use of novel liquid propellants. The key features of this effort were (1) the simplicity of the design as a result of the choice of propellants, (2) the novel environmentally friendly liquid propellant formulations, (3) the detailed modeling effort to be coordinated with the design and testing of the micro-propulsion system, (4) the micro-scale combustion and fluid dynamics diagnostics to be applied during testing and evaluation, and (5), the fabrication of micro uni-body combustion chambers and nozzles from ceramics using stereolithography techniques.

Results

During this program, progress has been made in the following areas: (1) combustion of gaseous hydrocarbon fuels and liquid monopropellants in small volumes using vortex flows to improve combustion stability and minimize heat losses, (2) electrolytic gasification and decomposition of liquid propellants as a means for ignition while minimizing power requirements and system complexity, (3) fabrication of axisymmetric ceramic thrusters for high temperature operation and materials compatibility with propellants and silicon based control modules, (4) testing and diagnostics of the ceramic thrusters, and (5) numerical model development for analysis and engineering design of the combustion chambers and thrusters. Highlights from each of these areas are briefly described below followed by a discussion of their significance to the present program. Additional results can be found in the papers and presentation material listed at the end of this report.

Asymmetric Whirl Combustion in Small Volumes

As combustion volumes are reduced in size, issues of residence time (finite-rate chemistry), fluid mixing (laminar flows, small length scales), heat loss management (high surface to volume ratios), and wall quenching of gas-phase reactions become increasingly more important. In the present program, many of these issues are addressed by application of the asymmetric whirl combustion concept [41,42] in which fuel is injected off axis of a rotating air flow. The concept of the asymmetric whirl combustor is shown in **Fig. 2**. Air flow enters the combustor tangentially without an axial component. The axial component is determined by mass conservation in which fresh mixture displaces the reacting mixture forcing it down the combustor axis. The air continues its rotating flow pattern by exiting tangentially or axially at the opposite end of the combustor.

Previous studies have been conducted on a large-scale combustor [41] which consisted of a closed horizontal, fused quartz cylinder, 61 cm in length and 88.9 mm in diameter. Fuel was injected through ports in a back plate of the cylinder. The tangential injection of air occurred only at the front end of the combustor where the fuel was injected. For symmetric injection, fuel was introduced at the center of the fuel back plate. For asymmetric injection, the fuel was introduced at the periphery of the back plate in a manner that the fuel and air inlet jets intersect. Experiments revealed that the fuel port could be anywhere along the periphery of the cylinder and not necessarily at the air inlet port. Because the asymmetric whirl combustor concept introduces fuel and air separately, the dangers and complexity of lean premixed combustion are avoided.

The swirl number, defined as the ratio of azimuthal momentum to axial momentum, was about 17. Typically, swirl combustors have swirl numbers of the order of 0.5-0.7. Thus, in contrast to conventional swirl combustors, the operation of the asymmetric combustor had circumferential velocities that greatly exceeded axial velocities.

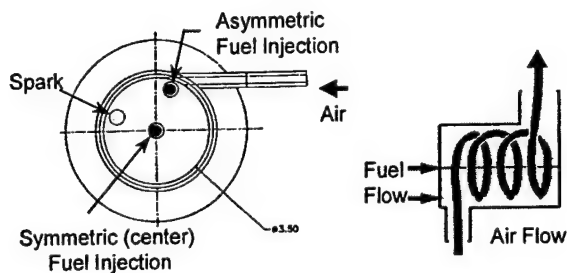


Figure 2. Whirl combustion concept illustrating both symmetric and asymmetric fuel injection.

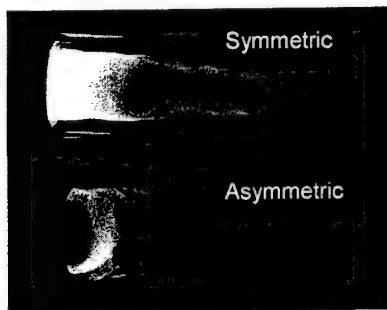


Figure 3. Symmetric versus asymmetric fuel injection (from Ref. 41).

Figure 3 presents photographs from Ref. 41 of two whirl flames produced by injecting 200 l/min of air and 6 l/min of methane into the combustor. The overall equivalence ratio for both types of injection was 0.286. Centerline (symmetric) injection of fuel produced an elongated, highly luminous, orange flame from 3-4 combustor diameters in length. However, by simply shifting the location of the fuel port to the periphery of the back plate, a blue, virtually non-luminous flame, only a single combustor diameter at most, was produced. In fact, the asymmetric whirl flame was not visible in the lighted laboratory. These differences in the flame structures are all the more unusual in view of the fact that neither the air nor the fuel inlet flow rates were altered to produce the effect. The pictures were taken during a single experiment by simply turning valves. Further, the asymmetric flame which viewed end-on appeared to have a hollow central region and a distributed reaction zone approximately $\frac{1}{2}$ cm from the quartz wall. No reaction was visible within the large central core.

The ring flame structure of asymmetric whirl combustion results from fuel injection into the region of highest turbulent kinetic energy of the whirling air flow, thereby producing rapid fuel-air mixing. The resulting flow produces a central hot combustion product core and a surrounding spinning outer flame zone with extremely good flame stability at low overall equivalence ratios.

Experiments have shown that the combustor exhibits an unusual wide range of stability margin, even for overall equivalence ratios below $\phi = 0.1$. The combination of tangential injection of air and tangential exit of combustion products appears to create a low-pressure trough along the centerline of the combustor. The Rayleigh criterion predicts that hot, low-density combustion product gases are trapped in this trough. This hot central core stabilizes the flame by acting as a source of enthalpy and radicals. Furthermore, the rotating flow internally re-circulates a portion of the hot combustion products into the fresh unreacted mixture entering the combustor, producing somewhat of a stirred reactor concept. The introduction of cold reactants about the circumference and the formation of the radial pressure gradient also enable the combustor walls to remain cooler than the hot central core.

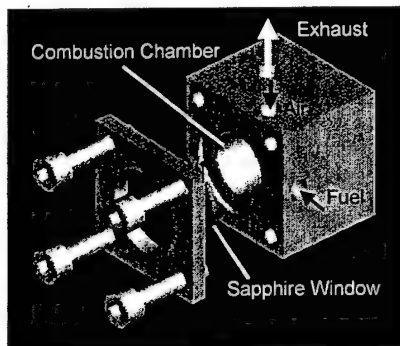


Figure 4. Meso-scale whirl combustor showing reactant inlet ports, exhaust port, combustor chamber and observational window.

Using this concept, meso-scaled combustors have been developed as shown in Fig. 4 as part of the present program with the intent that a similar combustion chamber geometry would be used for flame stabilization in the meso and micro scale thrusters. The largest meso-scale combustor fabricated has a diameter of 6 mm and a length of 6 mm. The overall combustor volume is approximately 170 mm^3 . For this combustor size, the inner diameter of the fuel jet tube was $500 \mu\text{m}$, while the inner diameter of the air jet tube was $760 \mu\text{m}$. Although the fuel jet enters the combustor perpendicular to the tangential air jet, the direction of the fuel jet is radially inward in the present meso-scale combustors vs. down the length of the combustor. However, the two jets still intersect immediately upon the separate flows entering the combustor. As shown below

from our three dimensional computational studies, the location and direction of the single fuel injector can impact the flame structure and dynamics.

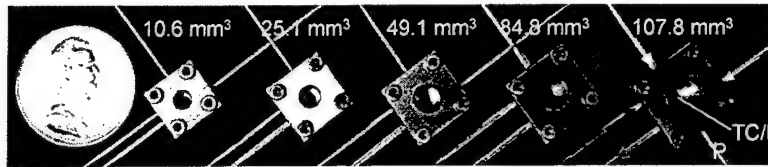


Figure 5. Meso-scale combustors for combustion scaling analysis. The hole at the back end of the combustion chamber is for igniter insertion.

A set of combustors, designed by scaling the Damköhler and Reynolds numbers and ranging in volume from 10 to 108 mm³, is shown in **Fig. 5**. Compared to the large-scale combustor described above [41], the smallest combustor shown in **Fig. 5** represents a decrease in volume by a factor of approximately 6×10^4 .

In experiments conducted to evaluate the meso-scale combustor flame stability and performance characteristics, fuel and air flow measurements were made with Hastings mass flow meters, which have been cross calibrated with results obtained from bubble meter measurements. The fuels tested were hydrogen (99.9 % purity), methane (99.5 % purity), and propane (98 % purity). Ignition was achieved by hot wire ignition using a 250µm diameter nichrome wire mounted on the end plate at the center of the combustor and also by spark discharge at the same location.

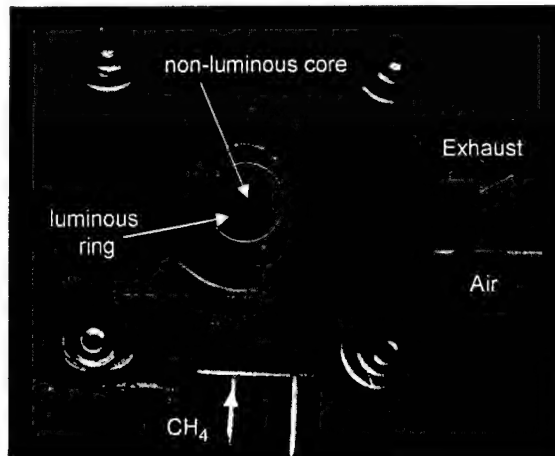


Figure 6. Meso-scale whirl combustion of methane air with an equivalence ratio of 0.85. The swirl number was 70. The Re number of the inlet air jet was 2800 and the Re number of the methane inlet jet was 220. The theoretical chemical input power was 97 W.

Lean and rich blow-off limits were obtained by fixing the air flow rate, igniting the combustor at a stable condition (typically at an overall equivalence ratio near 0.8) and then either decreasing or increasing the fuel flow rate until the reaction extinguished at which point the fuel

flow rates were recorded to determine the lean and rich limits, respectively. In the present context, equivalence ratio is defined for the entire combustion chamber volume. Since the fuel and oxidizer are injected separately into the chamber, the local equivalence ratio can vary from zero to infinity in the chamber.

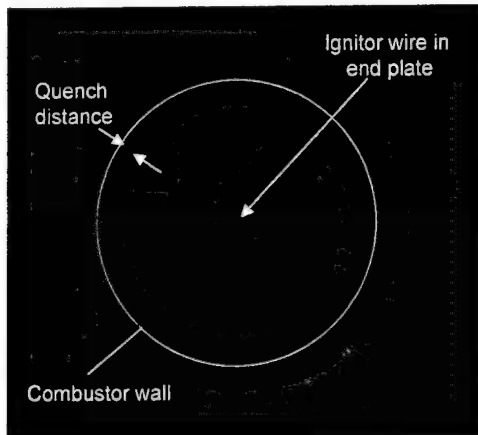


Figure 7. Meso-scale whirl combustion of propane air with an equivalence ratio of 0.8. The swirl number was 70. The Re number of the inlet air jet was 1780 and the Re number of the propane inlet jet was 310. The theoretical chemical input power was 50 W.

Initial experiments were conducted on hydrogen / air mixtures in the 170 mm³ combustor. Because of the superior flammability limits and low ignition temperatures of hydrogen, stable operation was observed over a wide range of air flow rates and equivalence ratios. The next fuel investigated was methane. An illustration of the combustor operating on a methane/air mixture with an overall equivalence ratio of 0.85 at atmospheric pressure is shown in **Fig. 6**. The combustion process appears as a spinning ring with a non-luminous core just as

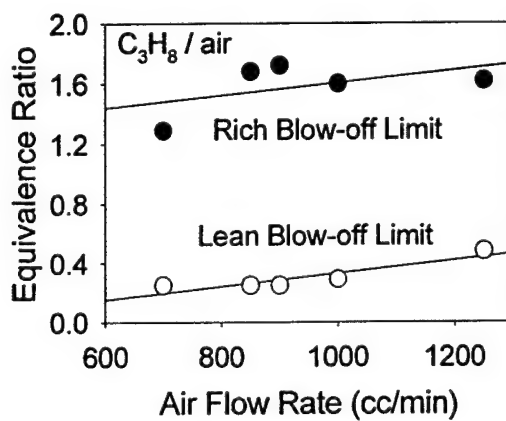


Figure 8. Stability limits for propane air combustion in the 170 mm³ meso-scale combustor.

observed in the larger scale combustor of Fig. 3. In the figure, the quench zone near the surface is approximately 0.5 mm thick.

An example of the combustor operating on a propane / air mixture with an overall equivalence ratio of 0.8 is given in Fig. 7. The flame again appears as a luminous blue ring with a non-luminous core. The quench layer is again approximately 0.5 mm thick.

Stable operation of the 170 mm³ meso-scale asymmetric whirl combustor has been achieved with mixtures of hydrogen and air, methane and air, and propane and air. Figure 8 gives the lean and rich blow-off limits as a function of air flow rate for propane as the fuel. Blow-off limits appear to increase with increasing airflow rate. Over the range of air flow rates investigated, the separation in equivalence ratio remains nearly constant. For propane, air flow rates were varied from 700 to 1250 cm³/min. At 700 cm³/min, the lean and rich blow-off limits were measured to occur at overall equivalence ratios of approximately 0.2 and 1.3, respectively. With an air flow of 1250 mm³/min, the lean and rich blow-off limits occurred at overall equivalence ratios of approximately 0.4 and 1.6, respectively. The lean and rich flammability limits, based on equivalence ratio, of propane in air are 0.56 and 2.7, respectively. Operation of the combustor on mixtures leaner than the lean flammability of a premixed mixture suggests that some stratification remains in the mixture during combustion.

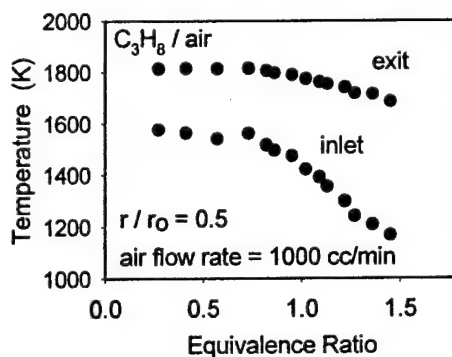


Figure 9. Temperature measurements for propane air combustion inside the 170 mm³ meso-scale combustor with an air flow rate of 1000 cm³/min at a radial position of $r/r_0 = 0.5$ for two different axial positions.

For fuel-lean mixtures, the flame appeared as a blue luminous ring. For fuel-rich mixtures, the flame was bluish-green. Under no conditions did the flame have a yellow emission characteristic of soot formation. Carbon deposits have also not been observed on any of the surfaces.

Temperature measurements as a function of equivalence ratio for propane as the fuel at an air flow rate of 1000 cm³/min are presented in Fig. 9. The measurements were obtained with a 76 μm diameter bare wire Pt/Pt-13%Rh thermocouple located at a radial position of half the radius at two axial locations, one near the reactant entrance and the other near the product exit. The measurements have not been corrected for radiation or conductive losses and coatings to prevent catalytic surface reactions have not been used. The adiabatic flame temperature for a propane air mixture with an overall equivalence ratio of 0.75 is approximately 1970 K. The inferred differences between measured and theoretical temperatures likely result from the heat losses of the meso-scale device, but could also result from incomplete combustion and uncertainties in the temperature measurements themselves.

Experiments on the meso-scale combustors ranging in size from 10 to 108 mm³ have been performed with H₂ / air mixtures. In all of these combustors, stable operation has been achieved with overall equivalence ratios ranging from approximately 0.3 to 7. At $\phi = 7$, extinction was not observed, but the hydrogen flow exceeded the limits of the fuel mass flow meter. An example of the chemical efficiency of the combustion process for three of the combustion

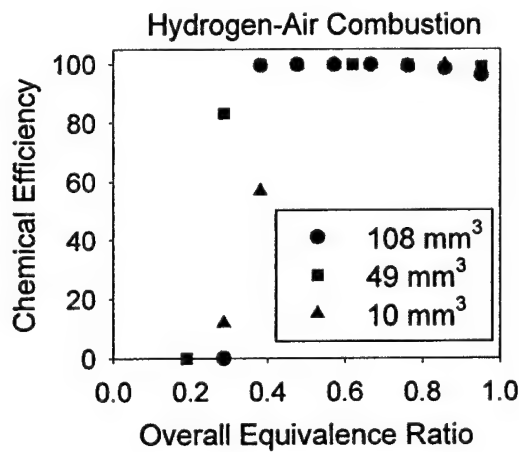


Figure 10. Chemical efficiency of hydrogen air combustion in different size combustors as a function of overall equivalence ratio.

chambers at a fixed residence time as a function of overall equivalence ratio is shown in Fig. 10. The chemical efficiency was determined by measuring the exhaust gas composition and considering what fraction of the original H₂ was converted to H₂O. These measurements were obtained by sampling the entire exhaust with an Aligent 3000A micro gas chromatograph (hydrogen, oxygen, and water vapor) and a Nicolet Nexus 670 Fourier Transform Infrared (FTIR) spectrometer (water vapor). Sample lines were heated and the composition measured without

drying the sample. At the lean blowoff limit, some scaling effects are observed with the smallest combustor having a slightly higher equivalence ratio at blowoff. However, once the overall equivalence ratio is above approximately 0.4, all combustors were extremely stable with chemical efficiencies approaching 100%. Based upon exhaust gas temperature measurements and comparison of these temperatures with the theoretical equilibrium value, thermal efficiencies were considerably lower, ranging from approximately 60 to 80%. No attempt was made to insulate the combustors.

Methane air combustion in the different sized combustors was also investigated and was found stable only in the largest combustor. Stable operation was achievable in all the combustor volumes with a small amount of oxygen enrichment to the air. **Figure 11** shows the chemical efficiency of the 10 and 49 mm³ combustors operating on an oxidizer mixture consisting of 40% oxygen and 60% nitrogen as a function of overall equivalence ratio for a fixed residence time. The chemical efficiency was determined from exhaust gas composition measurements using the FTIR. The species concentrations measured included CO, CO₂, CH₄, C₂H₂, C₂H₄, and C₂H₆ and chemical efficiency was determined by evaluating the fraction of carbon in the fuel that was

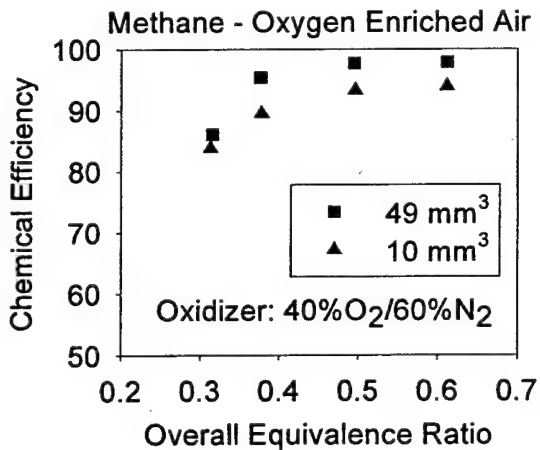


Figure 11. Chemical efficiency of methane oxygen enriched air combustion in different size combustors as a function of overall equivalence ratio.

converted to CO₂. Stable operation was achieved with overall equivalence ratios as low as 0.2. For overall equivalence ratios above 0.4, scaling effects were observed between the different combustors. In the present case, the 10 mm³ combustor had chemical efficiencies near 93% whereas the 49 mm³ combustor had chemical efficiencies near 98%. Further oxygen enrichment also showed a clear change in the flame structure and for the limiting case of pure oxygen, the flame appeared more as a micro diffusion flame stabilized at the tip of the fuel entrance jet. The change in flame structure resulted from the mixing time exceeding the chemical time. The pure

oxygen flame burns at a higher flame temperature and therefore the kinetics are considerably faster. In addition, for pure oxygen operation, the flow was achieved by simply eliminating the nitrogen in the oxidizer inlet flow. Therefore, the oxidizer jet momentum was reduced, which also increased the mixing time.

The above results were encouraging, particularly since air will not be the oxidizer used in the thruster. The asymmetric whirl combustion concept appeared to be a viable approach to sustaining gas-phase combustion in small volumes and the concept was implemented in the thrusters described below.

The actual thrusters are intended to operate on liquid propellants. In the present program, proof of concept studies were conducted to demonstrate that the combustors studied above would

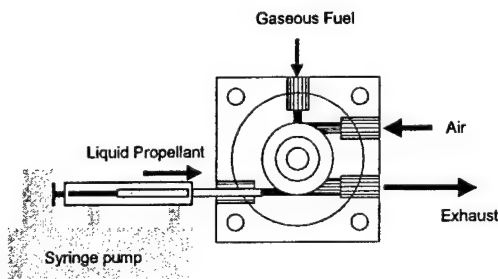


Figure 12. Schematic of tangential injection of liquid monopropellant into vortex combustion chamber.

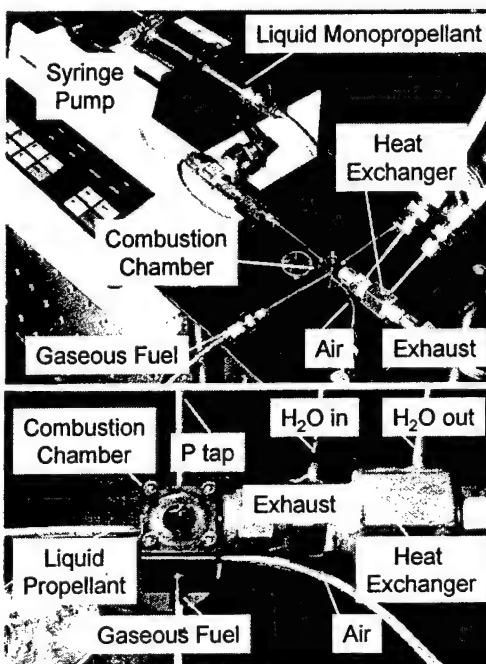


Figure 13. Experimental setup for liquid monopropellant injection initiated by gaseous fuel / air combustion.

operate on liquid propellants. As shown in Fig. 12, the present asymmetric combustion design was adapted for liquid monopropellant reactant flows. In the figure, the liquid reactant is injected tangentially into the combustion chamber just as the bulk air flow was in the gaseous reactant systems. However, in this configuration, the liquid flow can form a film along the surface of the combustor walls. This film may be used to cool the walls because of both endothermic liquid decomposition reactions and gasification, which can produce improved thermal management at the small scales of the present systems. For steady-state operation, the hot chamber walls and heat feedback from the gas-phase was used to continuously gasify the propellant. In the present work, the question of concern was, "Can the combustor operate on a liquid monopropellant, i.e., can a flame be stabilized in a small volume and can the simple liquid injection process provide a stable flowfield?" With the success of steady-state operation, the research will proceed to combine an ignition system (which is described below) to the combustion chamber.

Note that with the use of the monopropellant as the liquid fuel, mixing of fuel and oxidizer in the same phases or initially different phases is not necessary. Figure 13 is a photograph of the experimental setup illustrating the combustion chamber, the inlet and outlet, the exhaust heat exchanger, and the fuel syringe pump.

To demonstrate the capability to operate on liquid fuels, studies were initiated with liquid nitromethane, since it is a simple liquid monopropellant and its ignition and combustion behavior

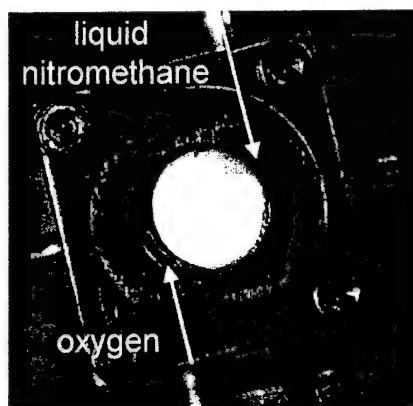
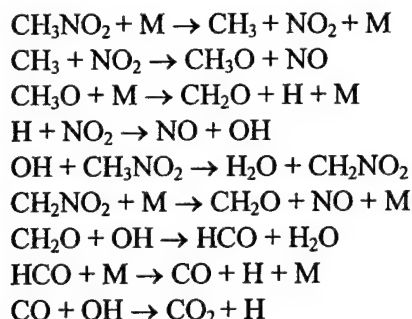


Figure 14. Combustion of 94% by volume liquid nitromethane / 6% by volume oxygen mixture. The emission of the nitromethane flame is a brownish bright white color as compared to the bright blue emission observed from the gaseous hydrocarbons. No carbon deposits or soot formation is observed in either case. The theoretical chemical input power was 97 W. The volume of the combustion chamber was 108 mm³ and the chemical power input was 160 W.

are relatively well understood. In future studies, the nitromethane will be replaced with a HAN based formulation. In these experiments, the 108 mm³ combustor was initially ignited on a methane / oxygen mixture with an equivalence ratio of approximately 0.5. Liquid nitromethane was then injected tangentially through another inlet port at the entrance of the combustion

chamber as shown in Figs. 12 and 13. Once the nitromethane flame was established, the methane gas flow was shut-off and the oxygen flow rate was decreased. For experiments operating at one atmosphere, it was found that the oxygen flow could not be completely shut off and still maintain combustion. The lowest oxygen concentration for which a stable nitromethane flame was achieved was 6 % by volume. The resulting flame is shown in Fig. 14 and produces a yellowish, bright-white emission. As in the combustion of the gaseous hydrocarbon / air mixtures, no soot or carbon deposits were observed to form on the surfaces. Thermodynamically, if the oxygen is eliminated from the mixture with 94% nitromethane, predicted flame temperatures decrease about 100 K.

Nitromethane, CH_3NO_2 , is a monopropellant that is relatively unreactive at one atmosphere in an inert environment. The need for the small amount of oxygen at one atmosphere can be understood by looking at its combustion kinetics relative to that of a hydrocarbon-oxygen system. The most important steps to nitromethane combustion are as follows:



Unlike hydrocarbon oxidation which has significant chain branching due to the presence

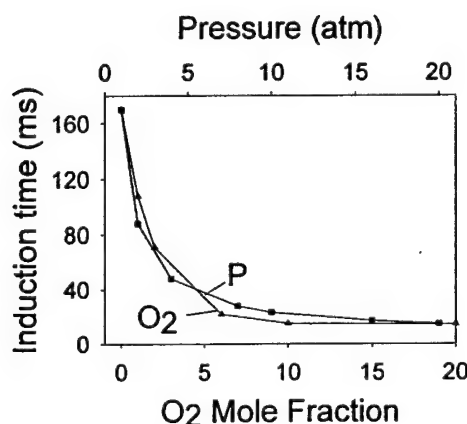


Figure 15. Homogeneous ignition of gaseous nitromethane as a function of pressure and oxygen perturbation.

of molecular oxygen (via. $\text{H}+\text{O}_2 \rightarrow \text{OH}+\text{O}$), no equivalent branching reactions occur in the nitromethane system. The main source of radicals is through pressure dependent dissociation reactions. Consequently, at low pressures, nitromethane kinetics are rather slow, but accelerate dramatically with pressure. Because of chain branching in hydrocarbon systems, reaction rates at low pressure can be fast and do not increase as much with pressure as in the case of nitromethane, which is often used to fuel racecars because of the strong dependence of kinetic rates on pressure. Note when nitromethane is burned in race cars, oxygen from the air is still used as an oxidizer. This is because nitromethane by itself is extremely fuel rich, with an equivalence ratio of 1.75.

In the atmospheric pressure experiments, the little amount of oxygen added to the system provides the initiation chain branching necessary at low pressure to achieve stable combustion. This added oxygen can be eliminated from the system by simply operating at higher pressures. The effect of an increased pressure on nitromethane kinetics is shown in **Fig. 15**. In this figure, homogeneous gas-phase kinetics calculations were performed using a detailed reaction mechanism for nitromethane decomposition kinetics that we assembled. The O_2 line shows the induction time of a mixture with initially 100% nitromethane and the effect of adding a small amount of oxygen to the mixture. Induction time is used here mainly as an indication of reaction rate, i.e., the shorter the induction time the faster the chemistry. In the atmospheric pressure experiments, 6% oxygen was required to stabilize a flame. According to **Fig. 15**, this represents about a factor of 5 acceleration in the kinetics, relative to the mixture without oxygen. The pressure (P) line in the figure shows the effect of pressure on induction time of pure nitromethane. As with increasing oxygen, an increase in pressure also accelerates the kinetics.

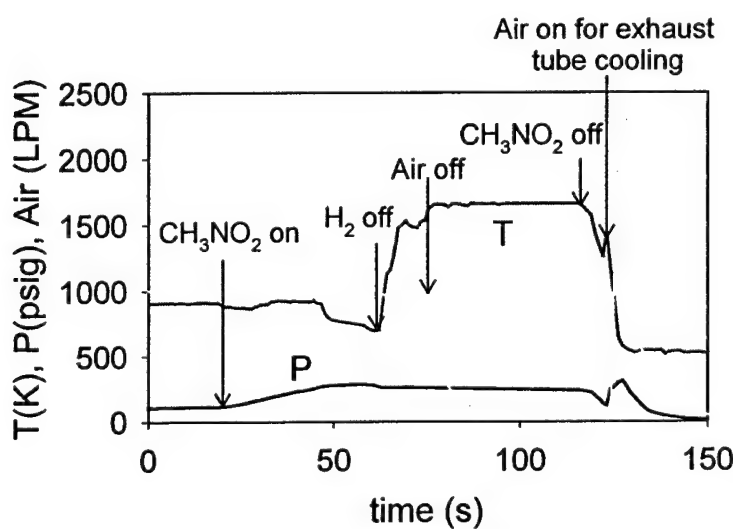


Figure 16. Steady-state operation of the 108 mm³ combustor on liquid nitromethane at 8 atm.

This figure suggests that a pressure of at least 7 atm would be required to stabilize the flame in the combustor (i.e., to achieve approximately the same induction time when 6% oxygen was added to nitromethane at atmospheric pressure).

In order to operate the combustion chamber at elevated pressures, the saffire observation window (0.5mm thick) needed to be replaced. This window was replaced with a solid inconel end cap that had a thermocouple, which protruded slightly into the combustion chamber. The thermocouple had a metal sheath, and thus experienced significant heat lost relative to the true gas phase temperature.

Figure 16 shows the successful operation of the combustor on 100% liquid nitromethane at a pressure of 8 atm. In the figure, the combustion process was initiated with a very lean hydrogen air mixture (temperature approximately 900K). As liquid nitromethane is added to the combustor, the hydrogen is first turned off and then the air is turned off. Stable combustion continued on pure liquid nitromethane. The experiments have been repeated at pressures above eight atmospheres and stable combustion has been achieved.

Model Development and Analysis of Vortex Flows

In order to obtain understanding of the flame stabilization and spreading process in small combustion chambers as well as to improve the chamber design, we have been developing three-dimensional codes for treating chemically reacting flows. The formulation is based on the three-dimensional conservation equations of mass, momentum, energy, and species transport for a multi-component system, and accommodates finite-rate chemical kinetics. Although we have developed the numerical code to implement detailed chemistry and transport, our initial calculations for hydrogen combustion have been based on a one-step reaction.

Currently, we are solving the governing equations through a density based, finite-volume methodology. The spatial discretization employs a fourth-order and a second-order central difference scheme for convective and viscous terms, respectively. The temporal integration is achieved using a four-step Runge-Kutta algorithm. Further efficiency is obtained by implementing a message passing interface (MPI) parallel computing architecture with a multi-block domain decomposition technique.

We have performed non-reacting and reacting flow calculations in an axisymmetric combustion chamber in which the reactants are premixed and are injected symmetrically about the circumference of the chamber at the front end plate and the exhaust gases exit symmetrically about the circumference at the end plate. In addition, we have performed non-premixed asymmetric flow calculations in which the air is injected from a single port tangentially at the

front end plate while the gaseous fuel is injected either perpendicular to the air flow or tangentially, parallel to the air flow, just as in the experiments described earlier.

Figure 17 presents some sample non-reacting flow results for axisymmetric injection and exhaustion of gases in the chamber. The length to diameter ratio of the chamber is 2, while the width of the inlet and exit ports, d , relative to the chamber diameter, D , is 0.2. The results show a series of flow patterns for different Reynolds numbers, defined as $Re = U_0 D / v$, where U_0 is the tangential injection velocity. At low Reynolds number, a recirculation zone is established at the front end of the chamber. With increasing Reynolds number, a second recirculation zone initially established at the exit end of the chamber merges with the front recirculation zone to establish a

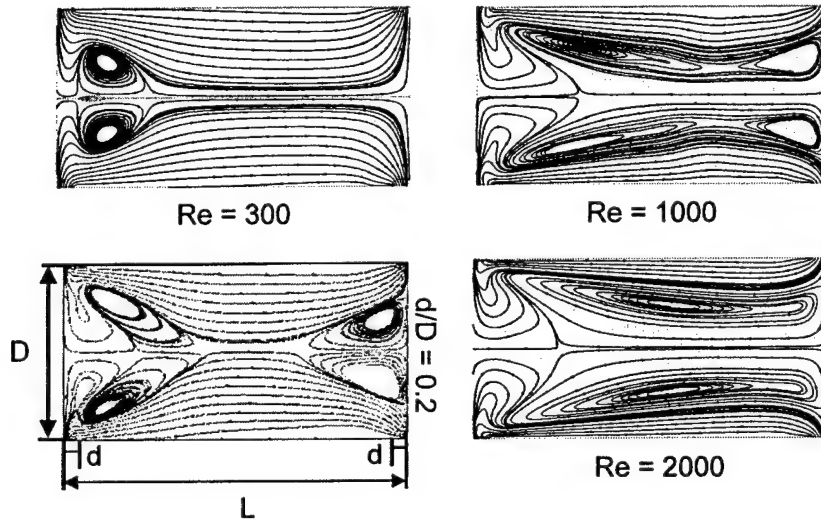


Figure 17. Streamlines for a non-reacting flow in an axi-symmetric vortex combustion chamber for a L/D ratio of 2 and various Reynolds numbers.

large recirculation zone. These zones establish the conditions for flame stabilization in the reacting flow. **Figure 18** illustrates another series of non-reacting flow results in which the L/D ratio of the chamber is changed from two to unity. A similar series of flow structures is observed. Clearly, the flow pattern is sensitive to both the overall combustion chamber dimensions as well as the flow conditions entering the chamber.

Figure 19 presents temperature and hydrogen mass fraction profiles as well as streamlines from a reacting flow calculation for a hydrogen / air mixture. The reactants are premixed and enter symmetrically about the front end of the combustor and exit symmetrically at the other end of the combustor. The combustion chamber had a diameter of 5.1 mm, a length of 5.9 mm, and gaseous inlet and exit widths of 500 μm . The inlet temperature was 300 K and the chamber pressure was 1 atm. The inlet tangential velocity was 262 m/s, with a small radial velocity component of 43 m/s. The equivalence ratio was stoichiometric. As seen in the figure,

the flame is stabilized in the leading recirculation zone and the hydrogen is consumed in a vortex ring that goes around the entire circumference of the chamber. In the center of the chamber, high temperature product gases recirculate with relatively low velocities.

The previous calculations have been performed to obtain fundamental understanding of the flow and flame structures under relatively simple flow conditions in the combustion chamber. In the present experiments, however, the reactants are not premixed and do not enter the chamber symmetrically. In fact, for hydrogen / air mixtures, premixing produces flashback into the 500 μm diameter inlet tubes.

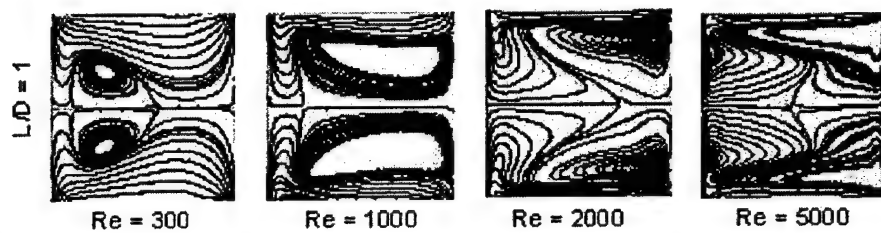


Figure 18. Streamlines for a non-reacting flow in an axi-symmetric vortex combustion chamber for a L/D ratio of 1 and various Reynolds numbers.

Figure 20 presents the calculated temperature field and particle trajectories for three different injection schemes. In all cases, the air was injected tangentially from a single port. The hydrogen injection positions included (1) perpendicular to the air jet and directed down the chamber, (2) perpendicular to the air jet and directed radially inward, and (3) parallel to the air jet and directed in the same co-flowing direction. For each case, the air and hydrogen flow velocities were 35.3 and 7.4 m/s, respectively, and the injection port diameters were identical for both

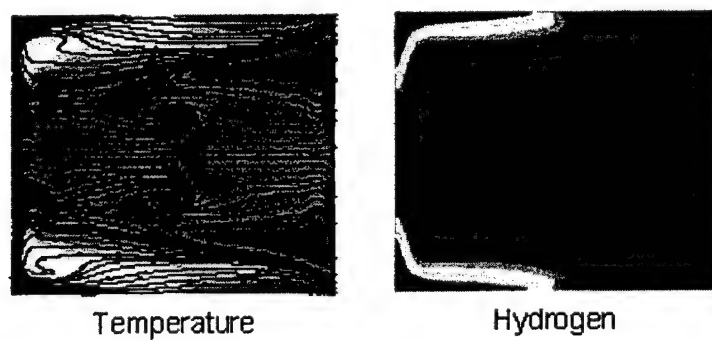


Figure 19. Temperature and hydrogen mass fraction contours and streamlines for a premixed reacting hydrogen / air mixture with axisymmetric injection.

flows. The chamber had a length of 5.9 mm and a diameter of 5.2 mm. The inlet flow temperatures were 300K, the chamber pressure was 1 atm and the overall equivalence ratio was 0.5.

The results show that in all three cases, recirculation zones are established in the core of the flow. Each case produced different mixing rates and internal flow structures, and consequently different temperature contours. However, the flow patterns were generally controlled by the larger volumetric air flow rates. The case where H₂ was injected axially downstream the cylinder produced the lowest peak temperature throughout the domain and fastest mixing. We are currently using results from these types of calculations to improve the design and operation of the small vortex combustion chambers. For example, based on these calculated results, we are now experimentally studying both perpendicular fuel injection axially down the chamber and tangential fuel injection. Preliminary results indicate even better flame stability in the smallest combustors, apparently because of better mixing and less disturbance to the centerline recirculation bubble formation.

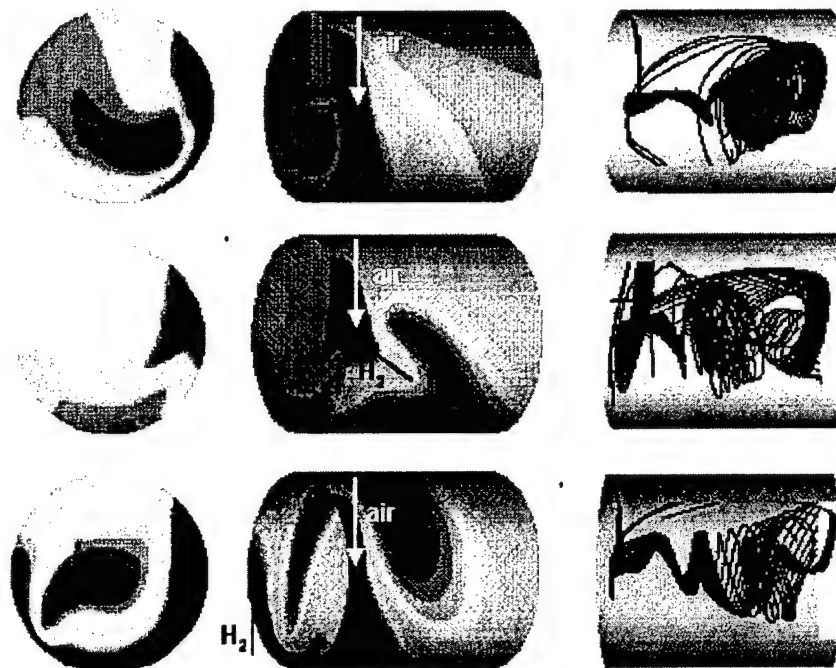


Figure 20. Temperature contours and particle trajectories for three different injection locations with the same tangential air injection location.

Electrolytic Ignition

Liquid homogeneous monopropellants are desirable for operation of the present micro-thrusters. The advantages of monopropellants are the simplicity of the resulting system design, reduction in hardware, and the ability of selecting the physical and performance properties of the propellant to fit the particular application. The propellant formulations include an energetic oxidizer, an alcohol fuel, and water as the liquid carrier. Hydrazinium nitroformate (HNF, $\text{N}_2\text{H}_5^+\text{C}(\text{NO}_2)_3^-$), ammonium dinitramide (ADN, $\text{NH}_4^+\text{N}(\text{NO}_2)_2^-$) and hydroxylammonium nitrate (HAN, $\text{NH}_3\text{OH}^+\text{NO}_3^-$) are solids with ionic structures that are water-soluble and serve as the primary propellant oxidizers. Various alcohols, also soluble in water, serve as the fuels. These types of formulations have been proposed and studied by others [43-46].

Considering the ingredients and products of combustion, the propellant formulations are expected to have good physical and environmentally friendly property characteristics for micro-spacecraft propulsion applications. The low to moderate flame temperature of these propellant formulations is an additional attractive feature for microscale applications. For nearly equivalent Isp levels as hydrazine, the resulting propellant densities are generally higher.

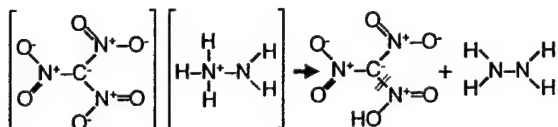


Figure 21. Initial thermal decomposition step of HNF is proton transfer with an effective activation energy of 20 kcal/mol. The decomposition products form hydrazine and nitrogen oxides such as NO_2 and HONO .

Compared to conventional hydrazine, HAN-based monopropellants are 40 percent denser, which offers a substantial volume benefit, and the freezing points of HAN-based monopropellants are less than 0°C , down to -65°C for some formulations, which will greatly reduce the power requirements for thermal management (tank and line heaters). HAN-based monopropellants do not pose a vapor hazard, are generally insensitive, and do not require extraordinary procedures for storage, handling and disposal. Thus HAN-based monopropellants offer considerable cost saving over N_2H_4 in terms of ground servicing [47]. Though using HAN-based liquid propellants have significant benefits over conventional hydrazine, such energetic salt-based fuels are often difficult to ignite [48].

In aqueous solutions, as the concentration of energetic oxidizer is increased in the formulations, the oxidizer forms ion-pairs [49] and the liquid becomes electrolytic. Proton transfer between the ion pairs generally initiates thermal decomposition. For HAN, when the

thermal decomposition of HAN-based liquid propellants. They found that the liquid propellant exposed to low energy electrolysis was easier to ignite by CO₂ laser than the liquid propellant not exposed to prior electrolysis.

In this effort, we have examined the electrolytic ignition characteristics of HAN-based liquid propellants. The experiments involved filament suspended micron-sized droplets. Voltage drops across two small electrodes inserted into the droplet were measured along with the resulting liquid resistance and power requirements necessary to achieve gasification and ignition. The propellants considered were XM46 and a HAN methanol mixture consisting of hydroxylammonium nitrate (HAN, 69.7 wt%), methanol (CH₃OH, 14.79 wt%), water (H₂O, 14.91 wt%), and ammonium nitrate (AN, 0.6 wt%).



Figure 23. Electrolysis of water (with 1 mol dm⁻³ NaOH) at atmospheric pressure. The voltage drop across the nichrome electrodes was 7 V.

The droplet chamber is shown in Fig. 22. The droplet is suspended by a bead at the end of a quartz fiber. Two nichrome (80%Ni/20%Cr) or platinum wires, with diameters of 250μm acting as electrodes, were inserted into the liquid propellant droplet. The gap between the two electrodes was varied, but was nominally of the order 1mm. During an experiment, a Hamilton syringe was used to suspend the droplet to the bead of the fiber. The electrodes were then moved

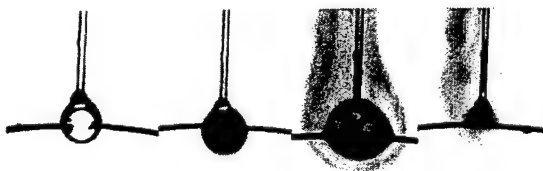


Figure 24. Electrolytic decomposition and gasification of a HAN/methanol/water droplet at atmospheric pressure with an applied voltage of 10 V across nichrome electrodes.

to the center of the droplet. A DC power supply was used to supply a controllable voltage drop ranging from 0 to 15V across the electrodes. By connecting the electrodes in a series circuit to a resistor, and then measuring the voltage across the resistor, the current through the droplet was determined. These voltages, including the voltages across the resistor and across the droplet were

recorded by a National Instruments data acquisition system. A Nikon Coolpix 990 digital camera and Sony digital video camera were used to record the droplet decomposition process.

As an illustration of the gasification process, **Fig. 23** shows the electrolysis of a liquid water droplet with 1 mol dm^{-3} NaOH. The applied voltage was 7 volts, which exceeds the voltage corresponding to the enthalpy change of 1.47 V. Once the voltage was applied (second frame), gaseous hydrogen bubbles were formed at the cathode and gaseous oxygen bubbles were formed at the anode. Continuous application of the voltage eventually consumed the droplet.

A similar, but more violent process was observed for the HAN-based propellants. In general, for both XM46 and the HAN methanol solution, results show that after application of a small voltage drop across two electrodes, the droplet begins to internally form bubbles, gasify, decompose (as indicated by a discolorization of the droplet), disrupt, and for XM46, ignite near the end of the gasification process. **Figure 24** illustrates the gasification/decomposition process of a HAN methanol water droplet. The first frame shows the droplet without the voltage applied, while the latter frames show different times of the droplet with 10 V applied across the electrodes. Note in the second frame the droplet size has increased and in the third frame, a gaseous decomposition zone is observed off the droplet surface with an elongated tail because of buoyancy effects. The gaseous reaction zone continues to appear (fourth frame) until the droplet is consumed. The color of the gas phase reaction zone was brown and likely associated with formation and reaction of nitrogen oxides. **Figure 25** illustrates the gasification / decomposition process observed with XM46. The frames show internal gasification, the overall size of the droplet to expand, then contract, and eventually lead to high temperature ignition of the droplet, as indicated by the bright flash in the last frame. The expansion and contraction process could

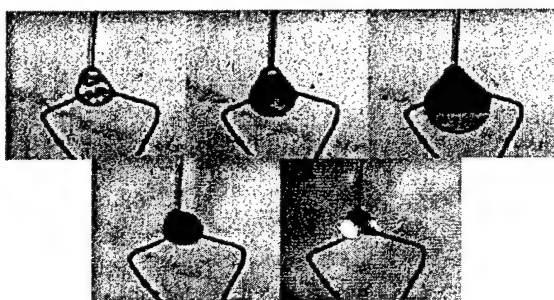


Figure 25. Electrolytic decomposition and gasification of a XM46 droplet at atmospheric pressure with an applied voltage of 10 V across nichrome electrodes.

occur many times with or without droplet fragmentation. Ignition at the end is likely associated with reaction of the TEAN.

When nichrome electrodes were used, small droplet fragments that were not consumed as a result of being jetted to the chamber windows were observed to have some green discolorization, likely revealing the presence of Cr_3^+ , which is green, thus indicating that the electrodes were chemically active. The activity of the nichrome electrodes can also be confirmed by some change in shape of the electrode tips after about 10 minutes of continuous electrolytic decomposition. Furthermore, some residue was generally observed to remain on the bead of the fiber after gasification for both XM46 and HAN-methanol. The color of the residue was brown-green for XM46 and light green for HAN-methanol. In addition, the residue from XM46 was thicker (more viscous) than that from HAN-methanol. From studies on the material compatibility of HAN-based liquid propellants [47,54,55] it has been reported that materials such as chromium or nickel will accelerate the decomposition of HAN-based liquid propellants. By replacing the nichrome electrodes with Pt, it was found that fewer residues were formed, the green discolorization of droplet fragments disappeared, and electrode erosion was nonexistent.

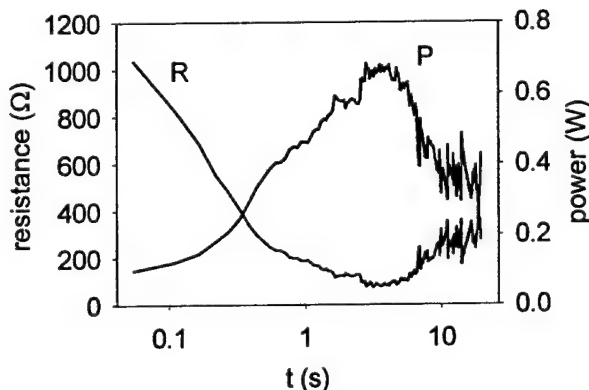


Figure 26. Resistance and power variation as a function of time for electrolytic gasification of a XM46 droplet with an applied voltage of 10 V across nichrome electrodes at atmospheric pressure.

During the initial phase of gasification, liquid resistances are high and power requirements are low (100's of μW). However, as the gasification process continues (e.g., after 50 ms), the resistance significantly decreases and the power requirement increases (100's of mW). **Figure 26** illustrates the variations of droplet resistance and power supplied to the droplet as a function of time for a XM46 droplet with a constant 10 V applied across nichrome electrodes. Since the voltage is constant, the decrease in resistance corresponds to an increase in flow of electrons, or an increase in the electrochemical reactivity. The decrease in resistance therefore corresponds to compositional changes of the droplet.

The effects of droplet voltage and electrode gap distance on the droplet resistance, gasification time, and droplet energy and power are shown in Fig. 27. For a particular electrode gap distance, the resistance and energy were found not strongly dependent on the voltage. However, increasing voltage yielded shorter gasification times and higher power input. Larger electrode gaps generally resulted in larger resistances, lower energies and powers, and longer gasification times. Figure 28 shows results of gasification time versus droplet voltage for HAN methanol droplets and platinum versus nichrome electrodes. The lowest gasification times in the figure yield droplet evaporation constants of about $0.5 \text{ mm}^2/\text{s}$. The energy supplied is equivalent to about 1/20 to 1/5 the energy required to electrolyze the approximately 0.15 weight percent of water contained in the droplet.

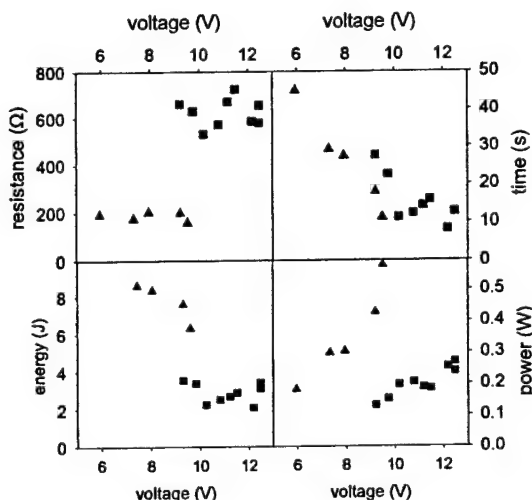


Figure 27. Effects of droplet voltage and electrode gap distance on the droplet resistance, gasification time, and energy and power supplied to the droplet for an XM46 droplet at atmospheric pressure (nichrome electrodes, initial droplet diameter approximately 1.5 mm). The diamonds correspond to electrodes with a smaller gap distance than the square symbols.

Considering water electrolysis first, it is well known that when a direct current is passed through water between two electrodes, water decomposes according to the overall reaction $\text{H}_2\text{O} \rightarrow \text{H}_2 + \frac{1}{2}\text{O}_2$ [56,57]. Water is actually a poor conductor of electricity and in order for this reaction to proceed a conducting electrolyte is generally added to the water. Water essentially dissociates into hydrogen and hydroxyl ions (H^+ and OH^-). The positive ions migrate toward the cathode, the negative electrode, where they are discharged by picking up electrons and forming hydrogen molecules, $2\text{H}^+ + 2\text{e}^- \rightarrow \text{H}_2$. The hydrogen molecules accumulate on the surface of the electrode until a bubble forms, and breaks away because of buoyancy or viscous shear stress. The electrode reaction requires intermediate catalytic reactions with the metal surface to form an

adsorbed layer of hydrogen atoms, which then recombine on the surface to form hydrogen molecules: hydrogen evolution starts with the proton discharge electrosorption reaction (Volmer reaction) $M + H_2O + e^- \rightarrow MH_{ads} + OH^-$, and is followed by both the electrode desorption Heyrovsky reaction $MH_{ads} + H_2O + e^- \rightarrow H_2 + M + OH^-$, and the recombination Tafel reaction, $MH_{ads} + MH_{ads} \rightarrow H_2 + M$. The net reaction is $2H_2O(l) + 2e^- \rightarrow H_2(g) + 2OH(aq)$.

At the oxygen electrode, the anode, a similar process occurs in which hydroxyl ions are discharged by giving up their electrons to the electrode and reacting to form water and oxygen. The oxygen molecules then accumulate into gas bubbles and must be broken away from the electrode surface. This reaction also requires intermediate catalytic reactions with the metal surface that yield the overall reaction, $2H_2O(l) \rightarrow O_2(g) + 4H^+(aq) + 4e^-$.

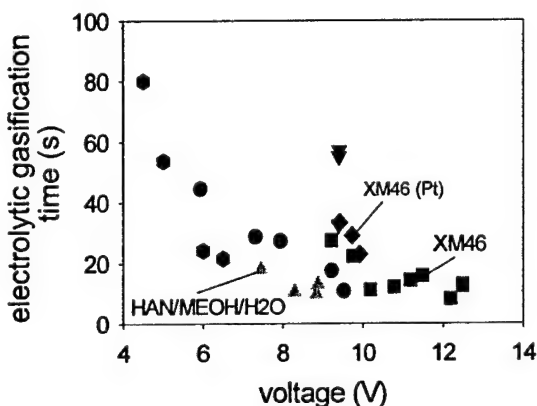
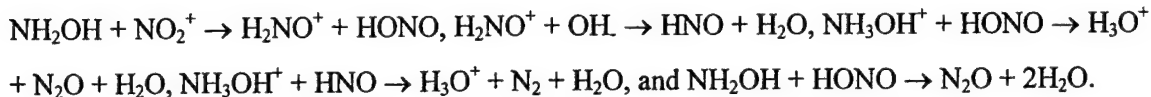


Figure 28. Electrolytic droplet gasification time for nichrome and platinum electrodes and XM46 and HAN methanol water droplets with initial diameters 1.5-2 mm in diameter at atmospheric pressure.

Hydrogen evolution at the cathode has an overall energy barrier of approximately 9.5 kcal/mol. In contrast, the thermal decomposition reaction of gas phase water, $H_2O + M \rightarrow OH + H + M$, has an activation energy of 118 kcal/mol. The overall process of water decomposition by electrolysis is the reverse of the process of hydrogen combustion. Therefore, the theoretical amount of energy required per unit quantity of hydrogen produced is the same as the heat of combustion. However, it is evident from the above activation energies that water dissociation by electrolysis can occur at a lower temperature than thermal dissociation.

The thermal decomposition of HAN is initiated by proton transfer, $HAN \rightarrow NH_2OH + HNO_3$, which is also believed to be the rate determining step in the condensed phase [58-60]. This step has an effective activation energy of approximately 15 kcal/mol. Thermal decomposition of HAN starts at temperatures near 80°C, but becomes significant at 120°C. The proton transfer reaction is followed by a sequence of secondary reactions including, $HNO_3 \rightarrow NO_2^+ + OH^-$,



Any mechanism that can compete with the initial proton transfer reaction of HAN should lower the decomposition temperature and accelerate the decomposition rate. Recognizing that water electrolysis produces H^+ and OH^- , new competitive steps with the proton transfer reaction such as $\text{NH}_3\text{OH}^+ + \text{OH}^- \rightarrow \text{NH}_2\text{OH} + \text{H}_2\text{O}$ and $\text{H}^+ + \text{NO}_3^- \rightarrow \text{HNO}_3$ or $\text{NO}_3^-(\text{aq}) + 4\text{H}^+(\text{aq}) + 3\text{e}^- \rightarrow \text{NO}(\text{g}) + 2\text{H}_2\text{O}(\text{l})$ and $2\text{H}_2\text{O}(\text{l}) + \text{O}_2(\text{g}) + 4\text{e}^- \rightarrow 4\text{OH}^-(\text{aq})$ likely become involved and thus alter the thermal decomposition mechanism. In addition, metal electrodes can participate in the electrolysis process. Nichrome electrodes, which consist of nickel and chromium, can undergo the oxidation reaction, $\text{Ni}(\text{s}) \rightarrow \text{Ni}_2^+(\text{aq}) + 2\text{e}^-$ at the anode and the reduction reaction, $\text{Ni}_2^+(\text{aq}) + 2\text{e}^- \rightarrow \text{Ni}(\text{s})$ at the cathode. HAN is very sensitive to metallics and surface phenomena and the presence of metal ions in the solution may assist the decomposition of HAN. Furthermore, these reactions will contribute to minimizing the power requirement necessary to initiate decomposition and gasification.

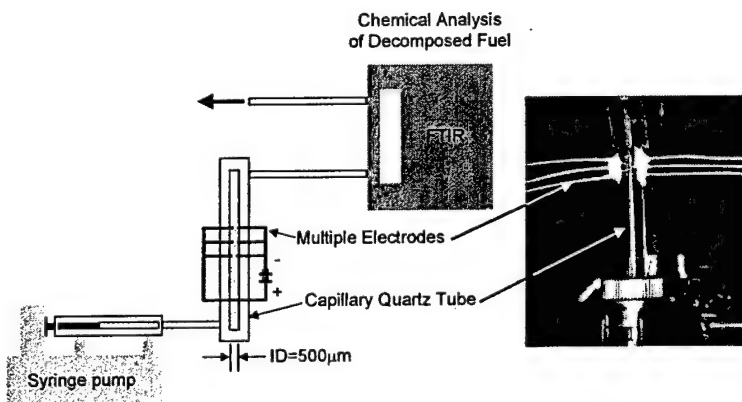


Figure 29. Experimental setup to study continuous flow electrolytic gasification and decomposition.

At atmospheric pressure, ignition of the high temperature secondary gas-phase reaction of HAN based propellants is generally not expected. The observations shown here are consistent with the thermal ignition studies of droplets by Farshchi et al. [61] and the strand burner studies of Chang et al. [62-64]. The thermal reaction generally required pressures above 12 atm to initiate the high temperature secondary reaction. As pressure is increased, the electrolytic decomposition voltage is expected to be proportional to the $\log P$, however, efficiency losses are generally less at higher pressure for a variety of reasons including the fact that the gas bubbles evolved are smaller and provide less hindrance to the passage of ionic current across the electrodes. Thus, it is anticipated that operation at higher pressures will even be more desirable for electrolytic ignition.

Furthermore, for very small thrusters, the electrolytic gasification rates may be sufficient for thruster operation without the high temperature gas-phase combustion. We are now studying the use of electrolysis in a continuous flow as shown in Fig. 29. In addition to measuring gasification rates and energy requirements, we plan to measure the decomposition products with Fourier Transform Infrared Analysis and compare these results to the gasification products from thermal heating.

Thruster Design and Fabrication

Materials selection, structural design, and micromanufacturing are essential technological resources that must be integrated with the chemical and mechanical aspects of the thruster development. A significant component to the present effort was the manufacturing of miniaturized ceramic components, which is important to high temperature operation at small scales. The thrusters were initially fabricated from alumina, but eventually will be constructed from Mullite. Compared to silicon, Mullite has a significantly lower thermal conductivity ($k = 6 \text{ W/m}^2\text{-K}$), a higher operational temperature limit (~1920 K) and a coefficient of thermal expansion similar to that of silicon ($5.4 \times 10^{-6}/\text{C}$).

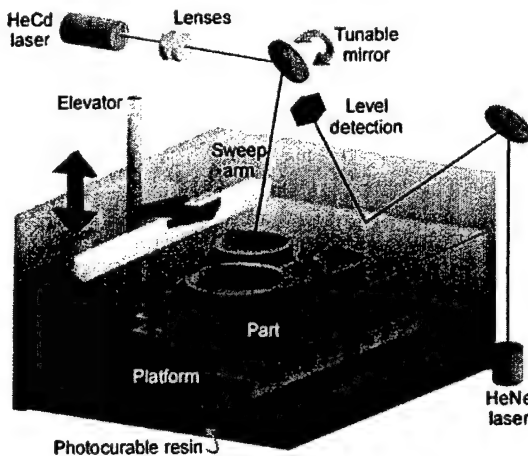


Figure 30. Stereolithography process

Three-dimensional stereolithography was utilized to manufacture the micro-thrusters. This process starts with the design of the part to be made as a three dimensional virtual solid in a computer aided design program. The solid is then sliced finely by another computer program

(Maestro) along the Z-axis, creating a build file that consists of a stack of X-Y layers. The build file is transferred to the build station used for the manufacture of the part; a schematic of this process is shown in **Fig. 30** (3-D Systems Inc. SLA-250, Valencia, CA). During the build, each layer is formed by raster scanning an ultra-violet laser across the surface of a photo-curable bath of liquid resin [67]. The solidified layer is moved down by one layer thickness inside the liquid bath so that the resin flows across the previously cured layer. The patterned curing process is then repeated to form the next layer on the top of the immediately previous layer. In this work, the resin is a highly concentrated colloidal dispersion prepared by dispersing alumina powder in an aqueous solution of ultraviolet curable polymers. The ceramic green body manufactured is subsequently dried, the photo-curable binder is burned out, and the part is sintered to full density.

The initial prototype design of the thruster was based on the asymmetric whirl concept and consists of a combined combustion chamber and nozzle. The chamber is open at the front end, but sealed by a gasket and manifold system to enable rapid development and testing of various reactant supply and ignition concepts in the combustion chamber. Several thruster bodies have been fabricated from aluminum oxide (**Fig. 31**). The ceramic thrusters have throat diameters ranging from approximately 300 - 700 μm , an exit area / throat area ratio of 2, and a conical nozzle divergence half angle of 14°. The combustion chamber has a volume of approximately 60 mm^3 . In addition, Inconel thrusters (**Fig. 32**) have been fabricated using electric discharge machining (EDM) for comparison studies with the ceramic thrusters.

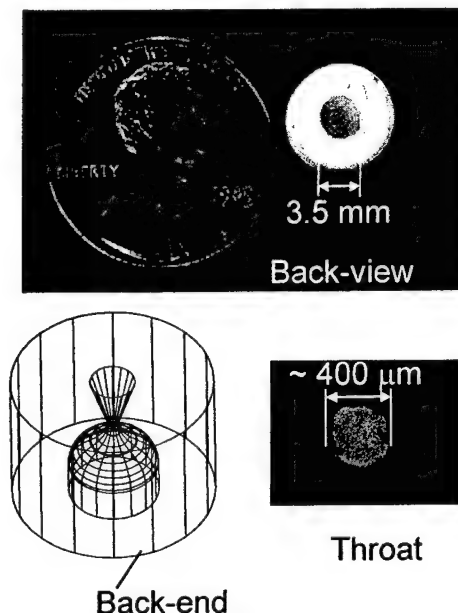


Figure 31. Alumina thruster body (top), wire-frame of thruster body (bottom left) and cross-section of throat (bottom right).

Pressure loaded small Inconel flanges (Fig. 33) are mounted at each end of the thruster to seal the combustion chamber and provide a means for injection and ignition of the reactants. A pressure tap (P), a thermocouple port (TC), and an igniter port are also positioned in the upstream (back) flange. Tangential ports at the upstream end of the combustor are available for gaseous air injection and liquid monopropellant injection. Gaseous fuel injection occurs perpendicular to the air injection port. High temperature gaskets are used to seal the thruster bodies with the upstream flange.

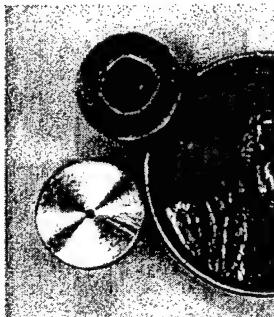


Figure 32. Inconel thruster bodies fabricated by EDM.

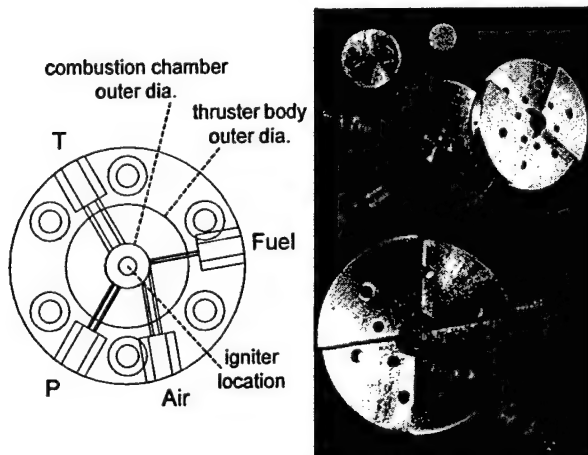


Figure 33. Schematic of the back flange (left) for hot flow test showing the locations of gaseous air and fuel injection, pressure tap, and thermocouple and igniter insertion points. Photographs of the front and back flanges for cold flow tests (right).

A second family of thrusters wasdesigned incorporating recent results from our own studies and those reported in the literature. These thrusters are to be fabricated by building the chamber from stereolithography followed by micro drilling of the throat orifice. We currently believe this will enable smaller throat diameters with much tighter tolerances. We are also building nozzles with significantly different expansion and contraction ratios. There has recently

been considerable discussion to the limited benefits of high expansions ratios in micro nozzles. For example, recent modeling results have shown that in silicon thrusters, the thruster body, which quickly attained a uniform temperature, provides a significant heat path for transporting energy from the combustion chamber and converging portion of the nozzle to the diverging section thus increasing viscous effects in the diffuser boundary layers. This research also reported that in planar nozzles etched from silicon, the large flat surface would lead to significant heat losses from the combustion chamber limiting the lifetime of combustion chamber and overall efficiency. These results further demonstrate the benefits of axisymmetric nozzles and the use of Mullite as the chamber body.

Thruster Operation and Characterization

Both cold flow and hot fire combustion experiments have been conducted on the prototype thrusters. Shadowgraph and schlieren techniques have been used to visualize thruster plumes. **Figure 34** shows shadowgraph (top) and schlieren (bottom) images of plumes from ceramic thrusters operated under cold flow conditions with helium. In the initial thrusters, plume trajectories have had some variation from thruster to thruster. The cause of the trajectory variations is currently being investigated.

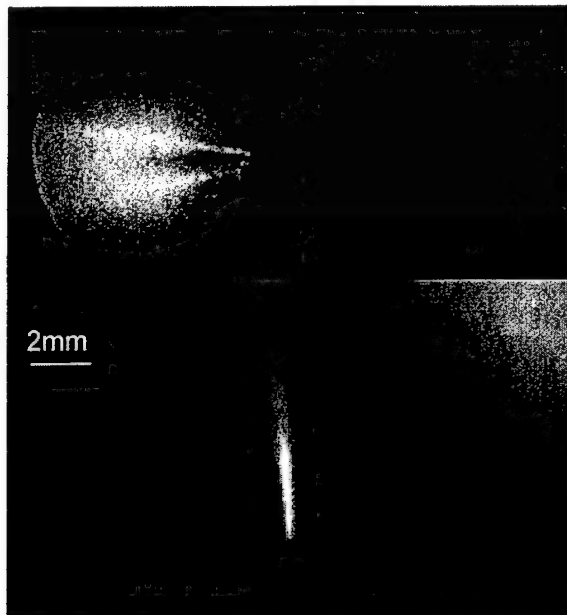


Figure 34. Shadowgraph images (top) of plumes from two different ceramic thrusters with helium and a chamber pressure of 10 atm. Schlieren image (bottom) of helium plume from a third ceramic thruster with a chamber pressure of 7 atm.

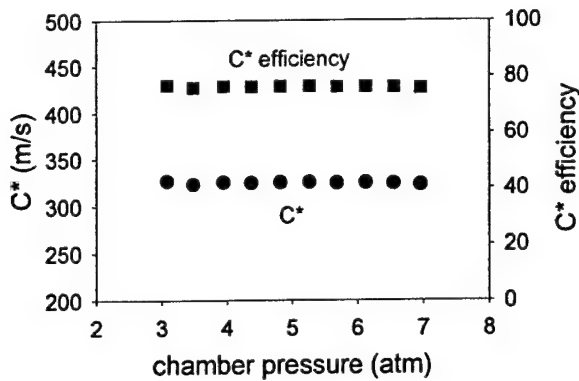


Figure 35. Characteristic velocity and C^* efficiency for cold flow operation.

Examples of the measured characteristic velocity and C^* efficiency for one of the thrusters as a function of chamber pressure is shown in Fig. 35. For cold airflow conditions, C^* was approximately 325 m/s and remains nearly constant independent of pressure. For this particular thruster, C^* efficiencies were initially calculated to be about 80%. This lower than expected efficiency is now attributed to uncertainties in the measurement of the nozzle throat area. As seen in Fig. 31, the throat cross sections are not perfectly circular and additional microscopic measurements of the throat diameters have yielded slightly different results depending on the side from which the diameters are measured, i.e., from the diffuser exit or from the combustion chamber entrance. Characteristic velocity efficiency measurements from the

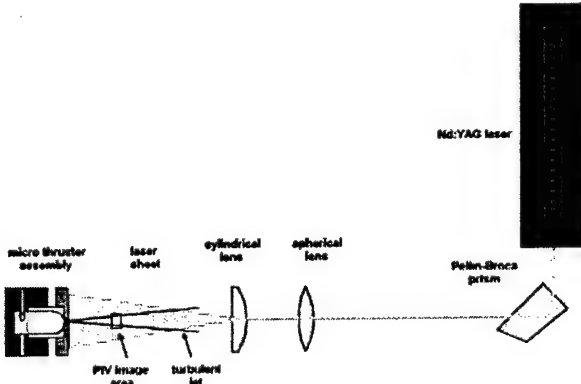


Figure 36. Schematics of the microthruster PIV experiment setup.

Inconel thrusters were $95 \pm 10\%$. Throat area measurements are currently being repeated for the ceramic thrusters.

Also in cold flow, Particle Image Velocimetry (PIV) was applied to map the velocity field in a plume produced by a thruster. The objective of the experiment was to demonstrate the feasibility and the potential of the PIV technique to study the micro-thruster jets.

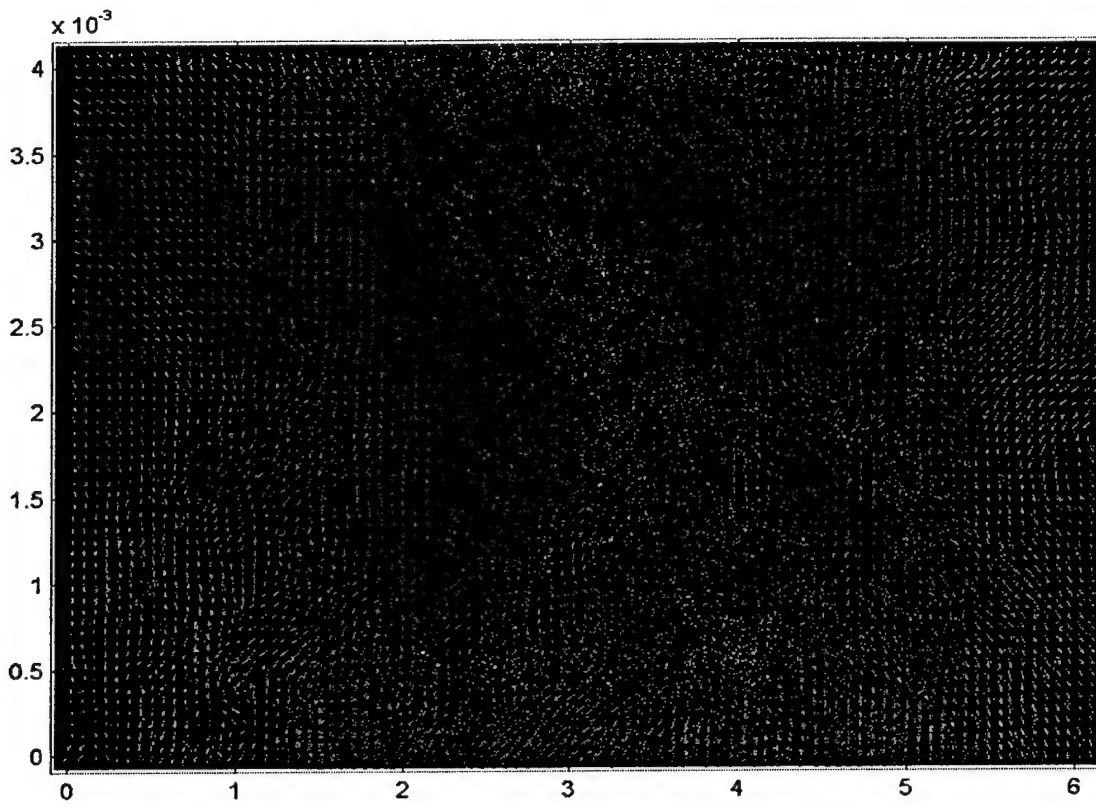


Figure 37. A double-exposed photograph of a 4 by 6.2 mm fragment the microthruster jet flow field centered on the point 3.5 mm downstream of the nozzle exit. The maximum velocity vector over the entire flow field corresponds to the local instantaneous velocity of 25 m/s.

The main components of the experimental setup are shown in Fig. 36. A Q-switched, double-pulsed, Nd:YAG laser with a harmonic generator, delivering a pulsed beam at the second harmonic wavelength of 532 nm was used as a light source. The separation between the two pulses was adjusted by precise timing of the laser flash lamp and the Q-switch, as the balance of the two pulses power was a function of the delay from beginning of the flash lamp discharge. The IR and the visible components of the laser beam were separated by a Pellin-Broca prism. A set of lenses (one cylindrical and one spherical) was used to produce a laser sheet with approximately 0.5 mm thickness at the waist. A mirror reflection was used to align the thruster housing with the laser sheet. A Kodak DSC 460 camera with a Micro-Nikkor 2.8/105 lens was used to acquire the PIV images. The camera CCD array provided the image spatial resolution of 3056 by 2031 pixels. The images were analyzed using an autocorrelation routine for 128x128 pixel cells extracted from the images. The cells were overlapping with a 32-pixel step in both directions.

In these experiments, the thruster pressure was theoretically chosen to match pressures at the nozzle exit. The experiments were conducted in ambient air and consequently the plume produced a helium jet that rapidly mixed with and decelerated into the surrounding air. The experimental conditions were determined by the characteristics of the micro-thruster flow. A sonic transition in the micro-thruster nozzle was produced by pressurizing the thruster combustion chamber to approximately 13 atmospheres with helium. This produced a rapidly decelerating jet of helium in the ambient air. The PIV image shown in Fig. 37 was centered on the point 35 mm downstream of the nozzle at its geometrical axis. The strong turbulent entrainment of the jet was used to deliver seeding material in the form of airborne sub-micron TiO₂ particles formed from TiCl₄, initially contained in a small vessel placed underneath the jet housing. A relatively high image magnification was required to resolve the turbulent length scale by having an acceptable level of particle displacement uniformity within each 128x128 cell of the double-exposed image. Positive results were obtained only when the image magnification was relatively high, equivalent to 470 pixels per millimeter. At such a setting, the effective field coverage in the object space was approximately 6.2 by 4.0 millimeters. A successful PIV velocity field reconstruction was accomplished using an image obtained under the conditions described above, with the delay between the laser pulses of 4.0 μ s.

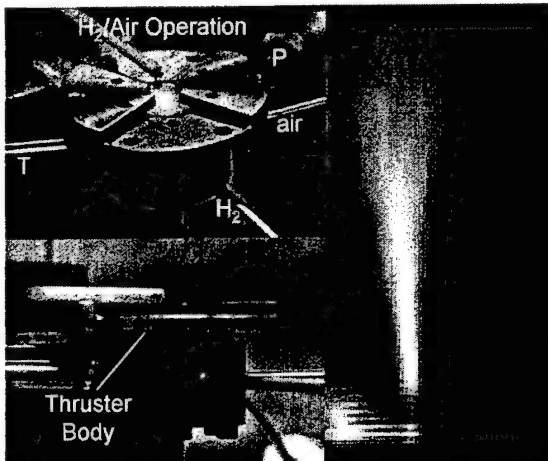


Figure 38. Thruster in hot fire operation with hydrogen air mixture. The thruster body in these pictures was reddish-orange in color (bottom-left), except for near the throat (top-left) where the surface was bright white. The image to the right is a schlieren image of the plume.

Experiments are planned to place the thruster in a vacuum chamber and obtain velocity measurements of the plume at different axial positions from the nozzle exit. These measurements, in addition to schlieren and shadowgraph photographic analysis, will be used to provide information on the flow exit Mach number, the degree of asymmetry in the flow and the

magnitude of any tangential velocity component remaining in the flow as a result of the high swirl number in the combustion chamber and large contraction ratio of the nozzle.

Hot fire tests without forced external cooling have been performed with H₂-air mixtures. Ignition was obtained via a spark across two small electrodes. Continuous operation for approximately one hour has been performed in addition to many start-up and shut-down sequences. Photographs of the thruster and the plume are shown in Fig. 38. The thruster body in these photographs appeared as a reddish-orange color. Surface temperatures of the ceramic thruster body from a thermocouple located on the top surface near the outer diameter of the thruster body (see Fig. 38) were generally near 600 K.

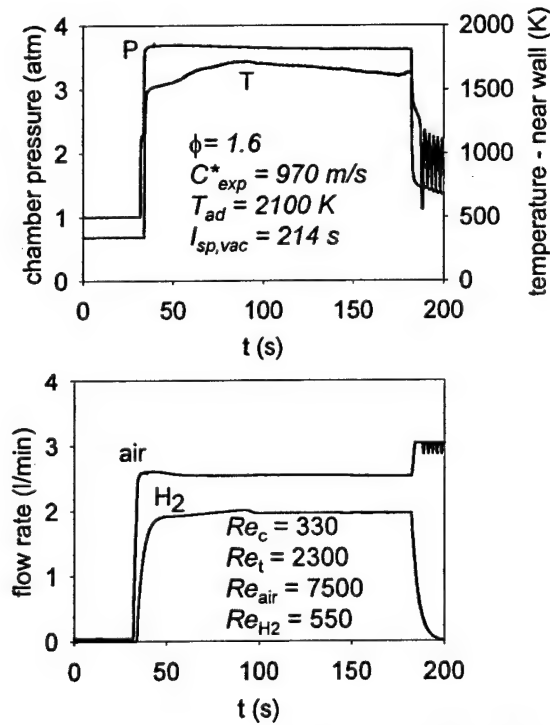


Figure 39. Start-up and shut-down of the thruster under hot-fire conditions.

An example of the start-up and shut-down of the thruster is shown in Fig. 39. Here the thruster is operated on a non-premixed H₂-air mixture with an overall equivalence ratio of 1.6. The chamber adiabatic temperature is calculated to be approximately 2100K. The Reynolds numbers of the inlet air, hydrogen, combustion chamber, and throat were, 7500, 550, 330, and 2300, respectively. For this condition, the experimental C* was determined as 970 m/s and the theoretical vacuum specific impulse was 214 s. The start-up procedure consisted of setting the air flow rate, followed by firing the spark, and then injecting the hydrogen. Ignition is rapidly achieved as indicated by the jump in pressure and temperature around 35s. The internal

temperature measurement is located at the upstream end of the combustion chamber near the combustor wall, but not in contact with the wall. The slight increase in chamber temperature at 90s is a result of a change in the hydrogen flow rate. Shut-down is achieved by closing the hydrogen flow to the chamber.

Figure 40 presents the measured C^* and C^* efficiency as a function of equivalence ratio for operation under hot fire conditions on hydrogen air mixtures. The characteristic velocity is observed to increase with increasing equivalence ratio and attain a maximum near an equivalence ratio of 1.5. In the figure, the C^* efficiency of the hot fire tests are plotted relative to the C^* efficiency of the cold flow tests to separate the inefficiencies of the cold flow from the combustion efficiencies. Since the low cold flow efficiencies are likely attributable to uncertainties in the throat area measurement, this presentation also removes this ambiguity. As can be seen from the figure, ratios of hot C^* efficiencies relative to cold C^* efficiencies are high, near 90% indicating good combustion efficiency and relatively small heat loss from the thruster.

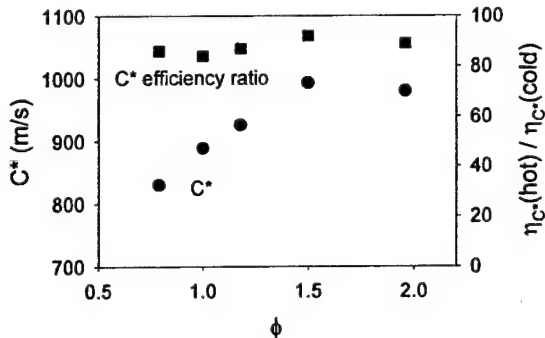


Figure 40. Characteristic velocity and the ratio of C^* efficiency under hot flow operation to C^* efficiency under cold flow operation.

Summary and Future Research

As highlighted in the discussion above, we have made significant progress on the development and analysis of several subcomponents of the meso- and micro- thrusters in this program.

In the area of asymmetric combustion in small volumes, we have:

- Demonstrated vortex flame stabilization in small volumes as a means to obtain sustained gas-phase combustion over a wide range of operating conditions and extended duration,
- Performed experimental scaling studies of combustion in small volumes ranging from 10 to 170 mm³,
- Demonstrated small volume vortex-combustor operation with non-premixed gaseous mixtures of hydrogen/air, methane/air, and propane/air, and
- Demonstrated continuous combustion of a liquid monopropellant.

These results indicate that the asymmetric vortex combustion process should be further optimized and continue to be considered as a mechanism for achieving combustion in small thrusters. Such combustion chambers may have usage in several other small-scale systems such as micro gas turbines, micro heaters, and micro reactors. Additional research and development is needed on the combustion of liquid monopropellants in these systems.

In the area of numerical modeling of combustion in small volumes, we have:

- Developed three-dimensional numerical codes for analysis of both non-reacting and reacting flows in small volume vortex combustion chambers,
- Performed cold-flow computational parametric studies to understand the detailed flow structures in vortex combustion chambers with various configurations, and
- Performed reacting flow simulations with gaseous hydrogen and hydrocarbons to study flame stabilization mechanisms and flame spreading processes.

These calculations revealed fundamental insight into the structure of small volume vortex flows and the flame stabilization mechanisms, and are now being used for design of the next generation of combustion chambers. Modeling of the thrusters can now be conducted routinely.

In the area of electrolytic ignition of liquid propellants, we have:

- Demonstrated electrolytic ignition concept as a means to gasify, decompose, and in some instances ignite HAN-based liquid propellants, and
- Characterized the electrolytic gasification and thermal decomposition of HAN-based propellants via suspended droplet experiments, photographic observations, and measurement of gasification times, droplet resistance and power consumption.

These results indicate that electrolysis is a viable means to gasify and decompose the liquid propellants in the small thrusters. The effects of pressure as well as continuous and pulsed flows in microchannels need to be further investigated, as well as the implementation of this technique into the micro thrusters.

In the area of fabrication and diagnostic testing of meso-scale ceramic thrusters, we have:

- Fabricated the first axisymmetric meso-scale thrusters from ceramics using stereolithography techniques,
- Characterized non-reacting and reacting meso-scale thruster operations via measurements of chamber pressure, chamber temperature, and characteristic velocity,
- Demonstrated thruster operation in both continuous and pulsed modes,
- Analyzed plume structure by shadowgraph and schlieren techniques, and
- Characterized downstream plume velocity vectors by particle image velocimetry.

The thrusters have been thermally cycled and operated under lengthy periods of time and have survived. Further research and development are needed to achieve better tolerances on throat dimensions. Furthermore, research and development are required to integrate the feed systems into the thruster bodies as well as in-situ diagnostics. For the present nozzle throat sizes investigated, combustion efficiency for hydrogen is very good. The operation of the thrusters on gaseous and liquid monopropellants must be demonstrated for implementation on operational spacecraft. Additional measurements are required, including thrust measurements, heat transfer measurements, and flow field diagnostics in the combustion chamber and the thruster plume.

Technology Transfer

In the microscale systems, electrolytic ignition is attractive because the electrical energy can be deposited directly into the liquid propellant and not into the system structure, for example, for catalyst heating. This is particularly important at the microscale because thermal management. Also, for microscale applications, power allotments could be propulsion systems is very low, and the ignition process needs to use as little energy as possible. Electrolytic ignition may also be more efficient than bed heating.

For high energy HAN based propellants, current catalysts used for ignition in macroscale systems have had survivability problems. Because of these failures, AFRL-Edwards became interested in determining whether electrolytic ignition could be applied to an Air Force high energy HAN based propellant and potentially replace the catalyst as an ignition source.

Under a separate investigation initiated from the present program, we have been studying two HAN-based liquid propellants (AF-M315A and XM46) in both stagnant and flowing experiments. A scale-up prototype of the electrode igniter system is given in Fig. 41. The

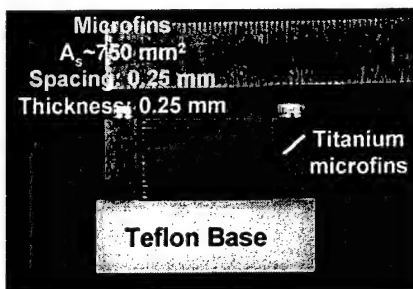


Figure 41. Electrodes for scale-up testing.

microfin electrodes were constructed from titanium having a total surface area of approximately 750 mm^2 per each fin while each microfin is spaced at 0.25 mm apart. These microfin electrodes are mounted to an isolation base made of Teflon. The microfin assembly was submerged in liquid propellant and a voltage potential was applied to the electrodes at various levels. Ignition and self-sustained combustion was achieved at atmospheric pressure. A series of selected images during the electrolytic ignition process for both AF-M315A and XM46 at atmospheric pressure are shown in Fig. 42. In these experiments, the voltage applied was 12 volts. The current flow varied with reactivity, but achieved values as high as 5 amps. As shown in the figure, once full ignition of the AF-M315A is obtained, an extremely luminous region was observed. In contrast, the second stage reaction was not evident for XM46. For XM46, tests were conducted at elevated pressures and the luminous second stage reaction was observed. Parameters being studied, which

affect the electrolytic ignition process, include fin separation distance, fin surface area, applied voltage and amperage, fin material, pressure, and propellant composition. Presently, a continuous-feed electrolytic combustor has been designed and fabricated to study the effectiveness of the ignition process stimulated by electrolytic-driven reactions during steady propellant flow through the electrode region. Based upon the results from the electrode experiments, the fin material and optimum fin spacing can be selected for the continuous-feed ignition system.

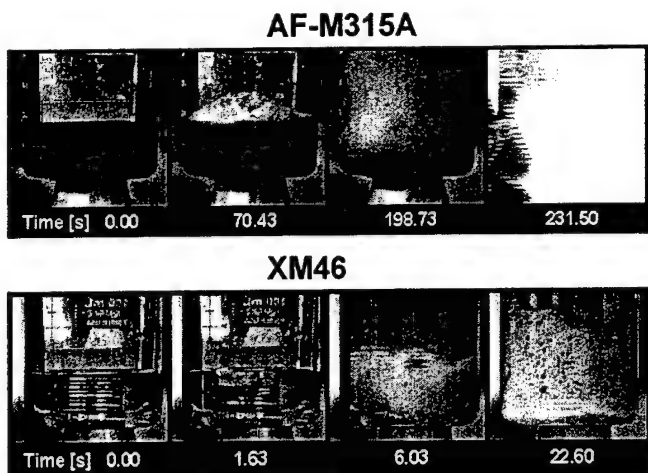


Figure 42. Electrolytic Ignition of AF-M315A and XM46.

Publications and Presentations

Listed below are presentations and publications from the current research effort.

- “A Liquid Propellant Microthruster for Small Spacecraft,” R.A. Yetter, V. Yang, D.L. Milius, I.A. Aksay and F.L. Dryer, Thirteenth Annual Symposium of the Propulsion Engineering Research Center, Huntsville, Alabama, 22-23 October, 2001.
- “Development of a Liquid Propellant Microthruster for Small Spacecraft,” R.A. Yetter, V. Yang, D.L. Milius, I.A. Aksay, and F.L. Dryer, pp. 3770380, 2001 Technical Meeting of the Eastern States Section of the Combustion Institute, Hilton Head, South Carolina, 2-5 December 2001.
- “Combustion Studies for the Development of a Liquid Propellant Microthruster,” R.A. Yetter, V. Yang, Z. Wang, Y. Yang, D. Milius, M. Peluse, I.A. Aksay, M. Angioletti, and F.L. Dryer, Fourteenth Annual Symposium of the Propulsion Engineering Research Center, State College, PA, 7-8 December 2002.
- “Development of Meso and Micro Scale Liquid Propellant Thrusters,” R.A. Yetter, V. Yang, Z. Wang, Y. Yang, D. Milius, M. Peluse, I.A. Aksay, M. Angioletti, and F.L. Dryer, 41st Aerospace Sciences Meeting & Exhibit, 6-9 January 2003, Reno, Nevada, AIAA 2003-0676.
- “Combustion Studies for Meso and Micro Scale Spacecraft Thrusters,” R.A. Yetter, V. Yang, Z. Wang, Y. Yang, D. Milius, I.A. Aksay, and F.L. Dryer, Third Joint Meeting of the US Sections of the Combustion Institute, The Combustion Institute, Chicago, IL, 16-19 March 2003.
- “A Numerical Study on Combustion Phenomena in Meso-scale Vortex Chambers,” Y. Wang, V. Yang, and R.A. Yetter, Eastern States Section of the Combustion Institute, Fall Technical Meeting, The Pennsylvania State University, University Park, PA, 26-29 October 2003.
- An Experimental Study on the Combustion Phenomena in Meso-scale Combustors, M.-H. Wu, R.A. Yetter, and V. Yang, Eastern States Section of the Combustion Institute, Fall Technical Meeting, The Pennsylvania State University, University Park, PA, 26-29 October 2003.
- Chemical Microthrusters: Combustion Issues and Approaches, R.A. Yetter, V. Yang, I.A. Aksay, and F.L. Dryer, Invited Paper, Eastern States Section of the Combustion Institute, Fall Technical Meeting, The Pennsylvania State University, University Park, PA, 26-29 October 2003.
- Combustion in Meso-scale Vortex Combustors: Experimental Characterization, M.-H. Wu, R.A. Yetter, and V. Yang, 42nd Aerospace Sciences Meeting & Exhibit, 5-8 January 2004, Reno, Nevada, AIAA 2004-0980.
- Numerical Study on Swirling Flow in a Cylindrical Chamber, Y. Wang, V. Yang, and R.A. Yetter, 42nd Aerospace Sciences Meeting & Exhibit, 5-8 January 2004, Reno, Nevada, AIAA 2004-0981.

References

1. Koeneman, P.B. Bush-Vishniac, I.J., and Wood, K.L., J. MEMS Systems 6, (4) 355 (1997). Nowak, R, "Batteries and Fuel Cells," MEMS Based Microscale Power Generation and Energy Conversion Concepts and Systems, DARPA Workshop, Arlington, VA, February 27-28, 1998.
2. Gad-el-Hak, M., "Microdevices-The Freeman Scholar Lecture," Journal of Fluids Engineering, 121, 5, March 1999.
3. Gad-el-Hak, M. "Challenges in the Understanding of Microscale Phenomena," AIAA 2003-439, 41st Aerospace Sciences Meeting and Exhibit, 6-9 January 2003 Reno, NV.
4. Helvajian, H., ed., Microengineering Aerospace Systems, The Aerospace Press, El Segundo, CA, and AIAA, Reston, VA, 1999.
5. Micci, M.M. and Ketsdever, A.D., eds., Micropropulsion for Small Spacecraft, Progress in Astronautics and Aeronautics, Vol. 187, AIAA, Reston, VA, 2000.
6. Fernandez-Pello, A.C., "Micropower Generation using Combustion: Issues and Approaches," Proc. Comb. Inst. 29, 883-899, 2002.
7. Chigier N. and Gemci, T., "A Review of Micro Propulsion Technology," AIAA 2003-670, 41st Aerospace Sciences Meeting and Exhibit, 6-9 January 2003 Reno, NV.
8. Janson, S.W., "Chemical and Electric Micropropulsion Concepts for Nanosatellites," AIAA 94-2998, 30th AIAA/ASME/SAE/ASEE Joint Propulsion Conference, Indianapolis, June 1994.
9. DeGroot, W.A. and Oleson, S.R., "Chemical Microthruster Options," AIAA 96-2863, 32nd AIAA/ASME/SAE/ASEE Joint Propulsion Conference, Buena Vista, FL, July 1996.
10. Mueller, J., "Thruster Options for Microspacecraft: A Review and Evaluation of Existing Hardware and Emerging Technologies," AIAA 97-3058, 33rd AIAA/ASME/SAE/ASEE Joint Propulsion Conference, Seattle, WA, July 1997.
11. Janson, S.W., Helvajian, H., and Breuer, K., "Micropropulsion Systems for Aircraft and Spacecraft," in Microengineering Aerospace Systems, ed. Helvajian, H., The Aerospace press, El Segundo, CA, 1999.
12. Janson, S.W., Helvajian, H., Hansen, W.W., and Lodmell, J., "Batch-Fabricated CW Microthrusters for Kilogram-Class Spacecraft," AIAA 99-2722, 35th AIAA/ASME/SAE/ASEE Joint Propulsion Conference, 20-24 June 1999, LA.
13. Rodgers, S.L., Carrick, P.G., and Berman, M.R., "Propellants for Microthrusters," in Microengineering Aerospace Systems, ed. Helvajian, H., The Aerospace press, El Segundo, CA, 1999.
14. Ketsdever, A.D. and Mueller, J., "Systems Considerations and Design Options for Microspacecraft Propulsion Systems," AIAA 99-2723, 35th AIAA / ASME / SAE / ASEE Joint Propulsion Conference and Exhibit, 20-24 June 1999 Los Angeles, CA.
15. Ketsdever, A.D., Wadsworth, D.C., Wapner, P.G., Ivanov, M.S., and Markelov, G.N., "Fabrication and Predicted Performance of Conical DeLaval Micronozzles," 35th AIAA/ASME/SAE/ASEE Joint Propulsion Conference, 20-24 June 1999, LA.
16. Ketsdever, A.D., "Microfluidics Research in MEMS Propulsion Systems," AIAA 2003-0783, 41st Aerospace Sciences Meeting & Exhibit, 6-9 January 2003, Reno, NV.
17. Sethu, P. and Mastrangelo, C.H., "Polyethylene Glycol (PEG)-based Actuator for Nozzle-Diffuser Pumps in Plastic Microfluidic Systems," Sensors and Actuators A 104, 283-289, 2003.
18. Rossi, C., Esteve, D., Temple-Boyer, P., and Delannoy, "Realization, Characterization of Micro Pyrotechnic Actuators and FEM Modeling of the Combustion Ignition," Sensors and Actuators A, 70, 141-147, 1998. Rossi, C., Esteve, D., and Minguez, C., "Pyrotechnic Actuator: A New Generation of Si Integrated Actuator," Sensors and Actuators, 74, 211-215, 1999.

19. Klintberg, L., Karlsson, M., Stenmark, L., and Thornell, G., "A Thermally Activated Paraffin-Based Actuator for Gas-flow Control in a Satellite Electrical Propulsion System," Sensors and Actuators A 105, 237-246, 2003.
20. Davis, T., XSS-10 Microsatellite Flight Demonstration Program, AFRL Technology Horizons, December 2004, p. 10.
21. London, A.P., Epstein, A.H., and Kerrebrock, J.L., "High Pressure Bipropellant Microrocket Engine," Journal of Propulsion and Power, 17, 4, 780-787, July-August 2001. London, A.P., Ayon, A.A., Epstein, A.H., Spearing, S.M., Harrison, T., Peles, Y., and Kerrebrock, J.L., "Microfabrication of a High Pressure Bipropellant Rocket Engine," Sensors and Actuators A, 92, 351-357, 2001.
22. Schneider, S., Boyarko, G., and Sung, C.-J., "Catalyzed Ignition of Bipropellants in Microtubes," 41st Aerospace Sciences Meeting and Exhibit, 6-9 January 2003 Reno, NV.
23. Yetter, R.A., Yang, V., Wang, Z., Wang, Y., Milius, D., Aksay, I.A., and Dryer, F.L., "Development of Meso and Micro Scale Liquid Propellant Thrusters," AIAA 2003-0676, 41st Aerospace Sciences Meeting & Exhibit, 6-9 January 2003, Reno, NV.
24. Hitt, D.L., Zakrzwski, C.M., and Thomas, M.A., "MEMS-based satellite micropropulsion via catalyzed hydrogen peroxide decomposition," Smart Materials and Structures, 10, 6, 1163-1175, 2001.
25. Platt, D., "A monopropellant milli-Newton thruster system for attitude control of nanosatellites," 16th AIAA/USU Conference on Small Satellites, Logan, UT, 12-15 August 2002.
26. Gibbon, D. and Baker, A.M., "Development of 50-100 milliNewton Level Thrusters for Low Cost Small Spacecraft," AIAA 2002-4150, 38th AIAA / ASME / SAE /ASEE Joint Propulsion Conference and Exhibit, 7-10 July 2002, Indianapolis, IN.
27. Lewis, Jr., D.H., Janson, S.W., Cohen, R.B., Antonsson, E.K., "Digital Micropulsion," Sensors and Actuators, 80, 143-154, 2000.
28. Rossi, C., Rouhani, M.D., and Esteve, D., "Prediction of the Performance of a Si-micromachined Microthruster by Computing the Subsonic Gas Flow Inside the Thruster," Sensors and Actuators, 87, 96-104, 2000. Rossi, C., Orieux, S., Larangot, B., Do Conto, T., Esteve, D., "Design, Fabrication, and Modeling of Solid Propellant Microrocket-Application to Micropropulsion," Sensors and Actuators A 99, 125-133, 2002. Orieux, S., Rossi, C., and Esteve, D., "Compact Model on a Lumped Parameter Approach for the Prediction of Solid Propellant Microrocket Performance," Sensors and Actuators, A 101, 383-391, 2002.
29. Lindsay, W., Teasdale, D., Milanovic, V., Pister, K., and Fernandez-Pello, A.C., "Thrust and Electrical Power from Solid Propellant Microrockets," Proceedings of the IEEE Fourteenth International Conference on MicroMechanical Systems, Interlaken, Switzerland, 606-610, 2001.
30. Reed, B., "Decomposing Solid Micropulsion Nozzle Performance Issue," AIAA 2003-0672, 41st Aerospace Sciences Meeting & Exhibit, 6-9 January 2003, Reno, NV.
31. Kohler, J., Bejhed, J., Kratz, H., Bruhn, F., Lindberg, U., Hort, K., Stenmark, L., "A Hybrid Cold Gas Microthruster System for Spacecraft," Sensors and Actuators A, 97-98, 587-598, 2002.
32. Ye, X.Y., Tang, F., Ding, H.Q., and Zhou, Z.Y., "Study of a Vaporizing Water Microthruster," Sensors and Actuators A, 89, 159-165, 2001.
33. Bruno, C., "Chemical Microthrusters: Effects of Scaling on Combustion," AIAA 2001-3711, 37th AIAA/ASME/SAE/ASEE Joint Propulsion Conference, 8-11 July 2001, Salt Lake City, UT.
34. Bruno, C., Giacomazzi, E., and Ingenito, A., "Chemical Microrocket: Scaling and Performance Enhancement," Final Report, SPC 02-4034, Contract No. FA8655-02-M034, AFRL, 25 July 2003.

35. Alexeenko, A.A., Gimelshein, S.F., Levin, D.A., and Collins, R.J., "Numerical Modeling of Axisymmetric and Three-Dimensional Flows in MEMS Nozzles," AIAA 2000-3668, 36th AIAA/ASME/SAE/ASEE Joint Propulsion Conference, 16-19 July 2000, Huntsville, Al.
36. Alexeenko, D.A., Levin, D.A., Fedosov, D.A., Gimelshein, S.F., and Collins, R.J., "Coupled Thermal and Fluid Analysis of Microthruster Flows," AIAA 2003-0673, 41st Aerospace Sciences Meeting and Exhibit, 6-9 January 2003 Reno, NV.
37. Kyritsis, D.C., Guerrero-Arias, I., Roychoudhury, S. and Gomez, A., "Mesoscale Power Generation by a Catalytic Combustor Using Electrosprayed Liquid Hydrocarbons," Proceedings of the Combustion Institute 29, 965-972 (2002).
38. Gemci, T. and Chigier, N., "Electrodynamic Atomization for MEMS Combustion Systems," AIAA 2003-675, 41st Aerospace Sciences Meeting and Exhibit, 6-9 January 2003 Reno, NV.
39. Stanchi, S., Dunn-Rankin, D., Sirignano, W.A., "Combustor Miniaturization with Liquid Fuel Filming," AIAA 2003-1163, 41st Aerospace Sciences Meeting and Exhibit, 6-9 January 2003 Reno, NV.
40. Ochoa, F., Eastwood, C., Ronney, P.D., and Dunn, B., "Thermal Transpiration Based Microscale Propulsion and Power Generation Devices," 7th International Workshop on Microgravity Combustion and Chemically Reacting Systems, NASA/CP-2003-21376, June 2003.
41. Yetter, R.A., Glassman, I., and Gabler, H.C., "Asymmetric Whirl Combustion: A New Low NO_x Approach," Proceeding of the 27th Symposium on Combustion, The Combustion Institute, Pittsburgh, PA, pp. 1265-1271, 2000.
42. Yetter, R.A. and Moore, D., "A Mesoscale Combustor based on Whirl Combustion," 12th Propulsion Research and Engineering Center Symposium on Propulsion, Ohio Aerospace Institute, Cleveland, OH, 26-27 October 2000.
43. Schöyer, H.F.R., Korting, P.A.O.G., Veltmans, W.H.M., Louwers, J., v.d. Heijden, A.E.M., Keizers, H.L.J., and v.d. Berg, R.P., "An Overview of the Development of HNF and HNF-based Propellants," 36th AIAA/ASME/SAE/ASEE AIAA Joint Propulsion Conference & Exhibit, Huntsville, Al., 17-19 July 2000.
44. Anflo, K., Grönland, T.A., and Wingborg, N., "Development and Testing of ADN-Based Monopropellants in Small Rocket Engines," A00-36427, 36th AIAA/ASME/SAE/ASEE AIAA Joint Propulsion Conference & Exhibit, Huntsville, Al., 17-19 July 2000.
45. Jankovsky, R.S., "HAN-Based Monopropellant Assessment for Spacecraft," AIAA 96-2863, 32nd AIAA/ASME/SAE/ASEE Joint Propulsion Conference, Lake Buena, Vista, FL, 1996.
46. E.J. Wucherer and S. Chrisofferson "Assessment of High Performance HAN-Monopropellants," 36th AIAA / ASME / SAE / ASEE Joint Propulsion Conference 16-19 July 2000, AIAA A00-36948.
47. B. Reed, "Material Compatibility Testing with HAN-based Monopropellants," 37th AIAA / ASME / SAE / ASEE Joint Propulsion Conference & Exhibit 8-11, July 2001, AIAA2001-3696.
48. A.J. Fortini and J.R. Babcock "High Temperature Catalyst Beds for Advanced Monopropellants," 37th AIAA / ASME / SAE / ASEE Joint Propulsion Conference and Exhibit, 8-11 July 2001, AIAA A01-34155.
49. N. Klein, "The Molecular Structure of the HAN-based liquid propellants," AD-A226 415.
50. Russel, S. and Fondrk, T.L., "Monopropellant Electrolytic Igniter," United States Patent 3,861,137, Jan. 21, 1975.
51. Vosen, S. R., "Concentration and Pressure Effects on the Decomposition Rate of Aqueous Hydroxylammonium Nitrate Solution," Combustion Science and Technology, Vol. 68, 1989, pp. 85-99.
52. Vosen, S. R., "The burning rate of Hydroxylammonium Nitrate-Based Liquid Propellants," Twenty-second Symposium (International) on Combustion, The Combustion Institute, Pittsburgh, PA, 1988, pp. 1817-1825.

53. Carleton, F.B., Klein, N., Krallis, K., and Weinberg, F.J., "Initiating Reaction in Liquid Propellants by Focused Laser Beam," Combustion Science and Technology, 88 (1-2): 33-41, 1993.
54. E. W. Schmidt, "Hydroxolammonium Nitrate Compatibility Tests with Various Materials --- A liquid propellant story," 1990 July, AD-A224 594 Ballistic Research Laboratory Report.
55. U.S. Department of Energy, "Technical report on Hydroxylamine nitrate," DOE/EH-0555 February 1998.
56. Jaksic, J.M., Vojnovic, M.V., and Krstajic, "Kinetic analysis of hydrogen evolution at Ni-Mo alloy electrodes", *Electrochimica Acta*, 45, 4151-4148, 2000.
57. M.F. Kibria, M.SH. Mridha and A.H. Khan "Electrochemical Studies of A Nickel Electrode for The Hydrogen Evolution Reaction," *Int. J. Hydrogen Energy*, Vol.20, No.6, PP. 435-440, 1995.
58. H.S. Lee, "A Study on the Thermal Decomposition of HAN-based Liquid Propellants," The Penn State University, Department of Mechanical and Nuclear Engineering, May 2000.
59. H.S. Lee and S.T. Thynell "Confined Rapid Thermolysis / FTIR Spectroscopy of Hydroxylammonium Nitrate," AIAA -1997, The Pennsylvania State University, 1997.
60. H.S. Lee and T. A. Litzinger, "Thermal Decomposition of HAN-based Liquid Propellants," *Combustion and Flame*, 123:2205-2222, 2001.
61. M. Farshchi, V. Vaezi, and B.D. Shaw "Studies of HAN-based Monopropellant Droplet Combustion," *Combustion Science and Technology*, 2002.
62. Y.P. Chang, J.K. Josten, B.Q. Zhang and K.K. Kuo "Combustion Characteristics of HAN/Methanol-Based monopropellants," 38th AIAA / ASME / SAE / ASEE Joint Propulsion Conference and Exhibit, 7-10 July 2002, AIAA2002-4032.
63. Y.P. Chang and K. K. Kuo "Assessment of Combustion Characteristics, and Mechanism of a HAN-based Liquid Monopropellant," 37th AIAA / ASME / SAE / ASEE Joint Propulsion Conference & Exhibit, AIAA Paper 2001-3272, 2001.
64. Y.P. Chang et al. "Combustion Behavior and Flame Structure of XM46 Liquid Propellant," *Journal of Propulsion and Power*, Vol. 17, No. 4, July-August 2001.
65. Garg, R., Prud'homme, R.K., Aksay, I.A., Liu, F., and Alfano, R., "Optical Transmission in Highly-Concentrated Dispersions," *J. Opt. Soc. Am.* 15, 4, 932-35, 1998.